The development of a Statistical Shape- and Finite Element-Model of the human pelvis to analyse the performance of current acetabular implants and validate the concept of a new deformable design

Nick Wassenberg, Vahid Arbabi (supervisor), Harrie Weinans (supervisor)

June 1, 2019

A B S T R A C T

Background: Patients who suffer from acetabular bone defects are often subjected to a decreased mobility and a loss of independence. To treat these bone defects, standard hemispherical acetabular implants offer in most cases the solution. However, when these defects are large, a custom triflange acetabular implant is needed. Although this type of implant performs well in general, it also has some drawbacks. These include higher costs and a longer design- and development cycle, since every implant is custom-made to the patient. In addition, it is expected that the triflange implant causes more stress-shielding (loss in bone-mineral-density (BMD) due to insufficient loads) than the standard implant. However, the evidence for this last statement is quite weak, since studies on both cups use different parameters,materials and environments.

Objective: The objective of this study is to determine if the custom triflange cup causes indeed more stress-shielding than the standard hemispherical cup. Furthermore, the goal is to find a solution for this and the other above-mentioned drawbacks of the custom triflange cup. Therefore, the goal is to study the potential of a deformable acetabular cup, which in theory should solve these issues of the triflange cup.

Methods: First a statistical shape model (SSM) of the human pelvis was developed to find patterns in defects of the pelvis, which could eliminate the need for customization. Next, a Finite Element (FE) Model with a bone-remodelling algorithm was developed to determine the difference in stress-shielding between the standard and the triflange cup. Furthermore, a FE model of a deformable implant is developed which is pressed into multiple defected pelvises. Finally, a machine-algoirthm is trained to predict the optimal deformable cup parameters, based on the type of defects.

Results: Several modes of deformation were found with the SSM, which were utilised in creating damaged pelvises for the Finite Element Model. Furthermore, it was found that the custom triflange cup decreases the BMD of the pelvis by 28.6% compared to pelvis without cup. With a deformable implant, this decrease can be reduced to 7.1%, which is in the similair range as the standard hemispherical cup. Finally, it was found that the machine-learning algorithm can successfully predict the optimal cup parameters, based on the type and size of defects.

1: Background

Healthy joints form an essential part of the human body and are a prerequisite to perform everyday tasks. Unfortunately, these joints can suffer from a loss in functionality caused by degenerative diseases or accidents [1],[2],[3]. As a result, patients are subjected to a decreased mobility and independency. which are some of the major values to patients [4].

Fortunately, there exist multiple solutions to treat a defect joint. To repair the defect, bone from the same individual who receives the graft can be used, referred to as autologous bone graft [5]. Autologous bone craft envolves the same procedure, with the difference being that bone is taken from another individual [6]. Both methods are not widely applied yet, due to the drawbacks and the complexity that comes with it. A more widely used approach is the use of orthopedic implants, which seem to be a reliable solution for damaged joints [7],[8]. Especially the hip joint is often replaced with an acetabular cup. If the current trend continues, it is expected that in 2030 around 572.000 total hip replacements are needed in the United States alone [9]. Furthermore, the amount of revision-operations for hip-implants (operations when the implant has reached the end of its lifetime and a new implant is required) is increasing with more than 30% from 2007 to 2013 [10]. This leads to an expected amount of almost 100.000 hip-revision operations in the United States in 2030 [9]. One of the causes for this increased amount of revision-operations is the longer life-expectancy of patients. A few decades ago less revi-

sions were needed, since the implant lasted long enough (on average 15 years [11], [12]) to assist the patient for the rest of his life. While the life-expectancy of patients is increasing, the lifetime of the implants is not increasing at a similair rate, resulting in a higher amount of revision operations.

One of the reasons that cause this implant-failure is loosening of the implant due to bone loss [13]. Insufficient bone may be present to fixate and stabilize the acetabular implant. To prevent this from happening, bone-loss should be minimized. With this in mind, it is important that the acetabular bone is sufficiently stimulated with mechanical loads. If this stimulus is below a certain value (typically strains below 1000μ-1500μ), bone-loss will occur [14],[15]. This phenomenon is referred to as stress-shielding and is a result of Wolffs law, which states that bone adapts to the loading it is subjected to [16],[17]. According to this law, the opposite (bone formation) occurs when the stimulus is above a certain value. This can be observed in tennis-players, whose dominant arm often contains thicker bone. Bone-loss on the other hand can occur in patients with acetabular implants. The implant shields the bone from stresses and strains, which result in bone-absorption. To minimize this effect, an implant material with a Young's modulus similair to the Young's modulus of bone should be chosen [18]. In addition, the shape and design of the implant can affect the strain/stress-distribution in the pelvis [13].

Depending on the type and degree of defects in the acetabulum, a suitable implant can be chosen. If the defects are relatively small or if the cartilage is degenerated, the common procedure is to implant an acetabular cup with a hemispherical shape, which mimics the natural shape of the acetabulum (figure 1). The diameter of this cup is usually a few millimeters greater than the diameter of the acetabulum. During surgery, the cup is hammered into the acetabulum and deforms. This deformation generates friction forces between the acetabulum and the cup, which stabilize the cup and keep it in place [19]. However, when large defects are present, insufficient healthy bone is left to allow this type of fixation. In these cases, a custom triflange implant is typically the solution. Compared to the standard cup, three flanges are added to the hemispherical cup, which are custom-made to fit exactly the pelvis of the patients (figure 2). Screws are used to fixate the implant on the locations of the screws.

Although the custom triflange cup provides a good solution for patients with large bone defects, it also has several drawbacks. Since the implant is custom-made, it is relatively expensive, compared to the standard hemispherical cup. In addition, it takes more time to design and prepare the implant [19]. For the standard hemispherical implant, 1 design with different sizes is sufficient for all patients with small bone defects. With the triflange implant, a new design is required for every case. Furthermore, it is expected that the flanges carry most of the load and shield the acetabulum from mechanical stimuli. The loads with the standard cup are centered at the acetabulum, while the triflange cup produces high loads on the bone which is in contact with the flanges (figure 1 and figure 2). This could lead to even further resorption of the remaining bone at the acetabulum, which is obviously undesired. The standard hemispherical cup on the other hand mimics the natural acetabulum, thus it is expected that this causes less stress-shielding in comparison with the triflange-implant. Several studies indicate that this is indeed the case by reporting lower strains in the acetabulum in case of a triflange implant compared to the standard hemispherical implant. Strain values for the triflange and standard implant are (after scaling for differences in parameters) in the range of 250-1700μ and 400-2000μ respectively, while stress-shielding occurs below strain values of 1000-1500μ. This would indeed indicate that more stress-shielding occurs with the triflange-implant [21],[22]. However, due to limited data and difference in parameter-values across studies, the evidence for this statement is quite weak.

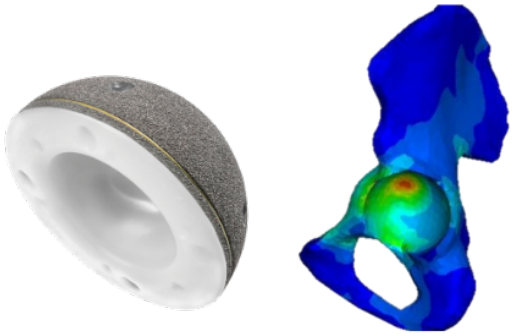

Figure 1: The standard implant with the corresponding load-distribution ([21])

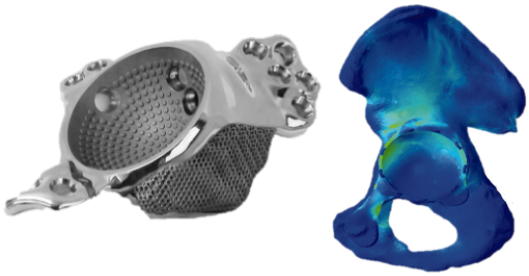

Figure 2: The triflange implant with the corresponding load-distribution ([25])

The need for a solution of above-mentioned drawbacks will become even more evident in the coming years. The costs for healthcare are increasing. In 2017 in the United states, the healthcare costs have risen faster than the average annual income [23]. Therefore, it is important to minimize healthcare costs off the custom triflange-implant. Furthermore, due to the relatively long design process for

each cup, it can take several weeks before the implant is ready for surgery. Finally, if the custom triflange cup indeed causes more stress-shielding, implants could last even less than the expected 15 years, as a result of bone-loss. With the increasing life-expectancy of patients, it is desired to increase the lifespan of the implants as well. This will in turn minimize the amount of revision operations, which are often complicated and pose high risk to the patient [24].

2: Objective

The main objective of this study is to improve the above-mentioned disadvantages of the custom triflange acetabular implant. This objective can be split up in several sub-objectives:

1. **Develop a statistical shape model (SSM) of the healthy and defect pelvis:** A statistical shape model is an analysis of geometrical properties of a shape by statistical methods. Developing a SSM of the pelvis can result in finding certain patterns among the acetabular defects, which could minimize the need for customization (and thus costs). This SSM is also used to generate pelvis-shapes for the finite element model (as highlighted in the next paragraph).
2. **Develop a finite element model (FEM) of the pelvis with both the standard cup and the custom triflange cup:** FEM uses partial and differential equations to solve amongst others stresses and strains. This can be used to study the differences in strains in the pelvis with the two types of implants, to test the hypothesis of increased stress-shielding with the triflange implant.
3. **Implement a bone-remodelling in the FE-model** A bone-remodelling algorithm can alter the bone-mineral density (BMD) of the pelvis based on the received strains. This allows exact quantification of the difference in stress-shielding between both implants.
4. **Validate the concept of a deformable implant as an alternative to the custom triflange implant:** A model of a deformable acetabular implant with a defect pelvis is developed to check if this design can solve the issues that occur with the custom triflange implant.

3: Method

The method is split-up into four main-parts, namely:

- The development of the Statistical Shape Model.
- The development of the finite element model (FEM) of the healthy pelvis
- The development of the finite element model of the defect pelvis (with the deformable implant)
- The implementation of the bone-remodelling-algorithms.

3.1: Development of a statistical shape model of the human hip

Healthy and damaged pelvises were acquired in order to built two statistical shape models (SSM), one to study the variations among the defect pelvises and one to study the variations among the healthy pelvises. A SSM which included both the healthy and defect pelvises was not developed since the variations between these two classes were too large. CT-scans of healthy pelvises were obtained from Utrecht medical center (UMC, Utrecht, the Netherlands). In total, CT-scans from 87 individuals were available for segmentation, which included both males and females between the age of 42 and 79 years old who still had an intact pelvis. From the majority of the CT-scans two pelvises, the mirrored left pelvis and the original right pelvis were selected and included in the SSM. Mirroring the left pelvis allowed the left pelvises to be compared with the right pelvises, in order to maximize the amount of data . Some pelvises were not included due to the presence of an implant or due to a reduced quality of the scan, which eventually lead to 155 pelvises which were included in the SSM of healthy pelvises. Defect pelvises have been obtained in the same manner from patients with a damaged acetabulum. CT-scans from defect pelvises were obtained from the catholic university of Leuven (KU Leuven, Leuven, Belgium). In total, 8 CT-scans from defect pelvises were available, which after mirroring and exclusion lead to 12 defect pelvises to be included in the SSM.

3.1.1: Image segmentation

Both healthy and defect pelvises were segmented from their corresponding CT scan by the use of the segmentation software Mimics 14 (Materialise Leuven, Belgium). Thresholding was performed by using the default Hounds-Field units values for Bone (CT) as provided by Mimics, which corresponded to values between 226 and 1799. Morphology operations were performed to close holes in the bone. Other bone regions connnected to the pelvis were disconnected by erasing connecting pixels, followed by a region-growing operation. Finally, the pelvises were smoothed with a factor of 0.8 to eliminate sharp edges.

3.1.2: Cutting operation

Due to the fact that patient-orientations in the CT-scanner were not identical, some pelvises contained more information then others, as can be seen in figure 3. In order to be

Figure 3: A difference in content between two (healthy) pelvises, caused by nonidentical orientations of the patients in the scanner

able to construct a SSM, this difference had to be eliminated. To achieve this, a cutting operation was performed. Since the global coordinate system was different for every case, a cutting plane was defined based on anatomical landmarks on the pelvis. First, three landmarks were chosen to define an initial plane in 3D-space (figure 4). The

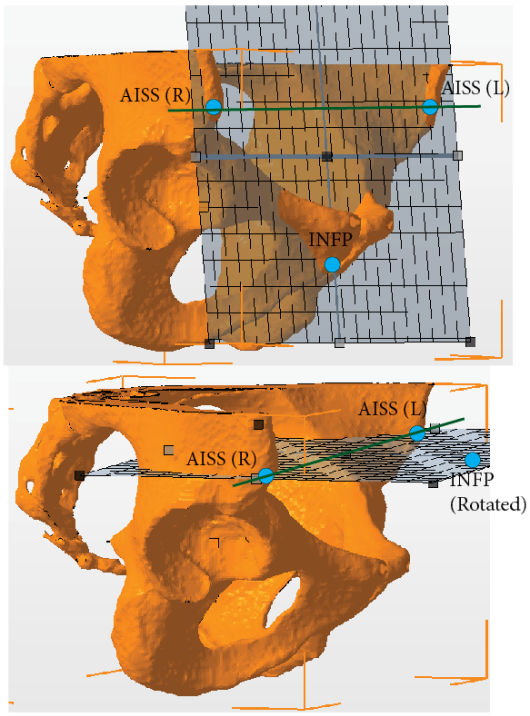

Figure 4: The initial landmarks in blue with their corresponding plane (top) and the landmarks with their corresponding plane after the rotation-operation (bottom).

selected landmarks were chosen in such a way that in the majority of the pelvises these regions could be identified, i.e. that this part of the pelvis was captured by the CT-scanner, in order to minimize the exclusion of pelvises. The selected landmarks consisted of the anterior inferior iliac spines (AIIS) on both side of the pelvises and the inferior pubis (INFP) [26].

In order to optimize the accuracy of the selection of landmarks, a curvature analysis was done in Meshlab (method = PCA)[27], as can be seen in figure 5. The selected landmarks describe the initial plane, which is not suited for cutting the pelvis since it will cut through the acetabulum, an important aspect of this SSM. To solve this issue, the plane was rotated with -96 degrees around the axis formed between the two AIIS landmarks, see figure 4. This can be described by a rotation matrix:

$$\text{INFP}_{\text{new}} = \begin{bmatrix} R(1)+R(2)+R(3) \\ R(4)+R(5)+R(6) \\ R(7)+R(8)+R(9) \end{bmatrix} \quad (1)$$

where

$$\begin{aligned}
R(1) =& (a*(v^2+w^2) - u*(b*v+c*w-u*x-v* \\
& y-w*z))*(1-cos(\theta)), \\
R(2) =& x*cos(\theta), \\
R(3) =& (-c*v+b*w-w*y+v*z)*sin(\theta), \\
R(4) =& (b*(u^2+w^2) - v*(a*u+c*w-u*x-v* \\
& y-w*z))*(1-cos(\theta)), \\
R(5) =& y*cos(\theta), \\
R(6) =& (c*u-a*w+w*x-u*z)*sin(\theta) \\
R(7) =& (c*(u^2+v^2) - w*(a*u+b*v-u*x-v* \\
& y-w*z))*(1-cos(\theta)), \\
R(8) =& z*cos(theta), \\
R(9) =& (-b*u+a*v-v*x+u*y)*sin(\theta), \\
\theta =& \text{The angle of rotation in radians (-1.6755 radians)} \\
a,b,c =& \text{The x,y and z-coordinate of the left AIIS landmark,} \\
& \text{respectively} \\
u,v,w =& \text{The x,y and z component of the vector which} \\
& \text{represent the rotation axis (normalized), respectively} \\
x,y,z =& \text{The x,y and z coordinate of INFP before rotation,} \\
& \text{respectively} \\
\text{INFP}_{\text{new}} =& \text{The x,y and z coordinate of the new (rotated) INFP}
\end{aligned}$$

After the rotation-operation only the coordinates of landmark INFP changed, since both AISS landmarks were located on the axis of rotation. With these three landmarks, a new plane is defined and the normal-vector is calculated. A Matlab script *(MATLAB Release 2017b, The MathWorks, Inc)* was written to speed up the described process (Appendix A). Finally, the pelvises were cut in Blender based on the orientation and location of the cutting plane.

3.1.3: Generating the reference shape

To be able to compare and align the cut pelvises, a reference shape has to be selected. Once this reference shape has been defined, the alignment and registration processes

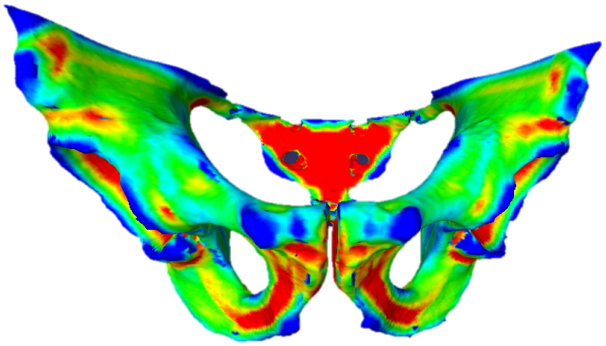

Figure 5: A curvature analysis to increase the accuracy of hand-picking landmarks.

can start. However, if one pelvis is selected as the reference shape, bias towards this selection could be introduced. To prevent this bias, a method is used where the reference shape is formed based on multiple iterations[28], as can be seen in figure 6. Initially, one of the training samples is chosen as the reference shape. Next, a small portion of the samples is selected and the SSM is built. The mean of the generated model is selected as the reference shape for the next step. This process is repeated until the difference between the reference shape from the previous step and the new generated reference shape is smaller than a predefined value, i.e. a steady state has been reached. Once this criteria has been met, this final reference shape is used during the building of the SSM.

3.1.4: Alignment of the samples

Due to the different orientations of the pelvises in the CT-scanner, variations in translation and rotation had to be eliminated in order to be able to determine the variance in shape and size. This objective can be described by a minimization problem, namely minimizing the distance between the generated reference shape and each sample. To do so, samples were first aligned by hand-picked landmarks, both on the reference shape and the new sample. For this procedure, a minimum of three landmarks is required to define the orientation in 3D-space. However, four landmarks were selected to minimize the error as a result of visual handpicking of the landmarks. The selected landmarks included the caudal margin of the pubic symphysis, the cranial margin of the pubic symphysis, the point along the obturator margin at the minimum breadth of the ischium and the most cranial point on the acetabular rim adjacent to the lateral iliac border [29]. This first step is done in Meshlab, where the total euclidean distance between every landmark on the new sample and their corresponding landmark on the reference is minimized. After the pre-allignment has been completed for every sample, alignment is performed based on uniformly selected points from the mesh cloud. Each point on the new sample is associated with the closest point on the reference shape. By applying both rotation and translation the new sample is transformed, according to the Procrustes analysis [30]. Multiple iterations are performed, until the difference between the new sample and the reference does not decrease anymore. After the alignment-phase, it was evident that there was still variation between pelvises at the location of the cut. This is most likely caused by minor errors while picking the landmarks for the cutting plane. In order to prevent modes of deviation at the cutting area, one final cut was made through all the aligned pelvises at the same coordinates in 3D-space.

3.1.5: Registration

The process of registration consists of registering corresponding points between the reference shape and the samples. This can be described by a deformation process between the reference shape and the samples. Based on these deformations (which are modelled as a Gaussian Proces) an optimization problem can be defined [31]:

$$u = arg_{\mu \epsilon F} min D[\Gamma_D, I_T, u] + \mu R(u) \tag{2}$$

Here Γ_D represent the reference surface, I_T describes the sample image and u is the transformation from the reference surface to the sample surface as a result of deformations F. Finally, R is a regularizer and D is a similarity transform.

3.1.6: Model evaluation

The principal component analysis [32] can now be used to define the main shape variations. From the covariance matrix, the eigenvectors and eigenvalues can be calculated, which correspond to the modes of variations and the amount of variance of these modes respectively. With this model, it is possible to describe in theory every shape with:

$$x = \overline{x} + \Phi b \tag{3}$$

Here, the shape of a pelvis x can be described by the mean shape of the pelvises ($\overline{x}$) plus the eigenvector matrix (Φ) multiplied with the vector of shape parameters (b).

To evaluate the accuracy of the model, the following aspects were calculated:

1. *Model generality:* How well can the model predict a pelvis which was not included in the training set. This is evaluated by leaving one pelvis out of the training and use that as input for the model [33]. The squared error between this output (X_i) and the actual pelvis (X_i') is then calculated:

$$G(M) = \frac{1}{n} \sum_{i=1}^{n} |X_i(M) - X_i'|^2 \tag{4}$$

2. *Model specificity:* To what extent is the output (X_i) similar to the samples in the training set (X_i') [28]:

$$S(M) = \frac{1}{n}\sum_{i=1}^{n}|X_i(M) - X_i'|^2 \tag{5}$$

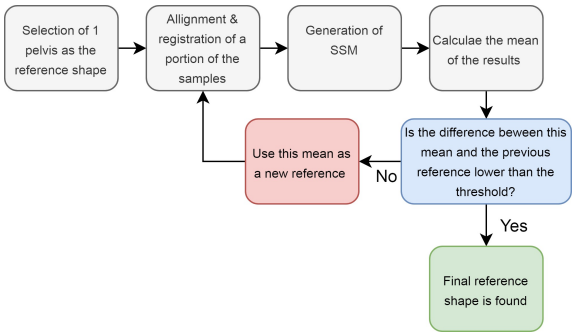

Figure 6: The iterative procedure to select the reference shape of the SSM

3.2: Development of the Finite Element Model for the healthy pelvis

To study the effect of several implant-designs on the stress distribution in the pelvis, a finite element model was developed in Abaqus. First, a standard analysis was run with a single loading-step, to get an idea on the load distribution in every case. Next, two bone remodelling algorithm were derived, validated and implemented to study the BMD after +- 1 year. This gives a indication of the relative stress-shielding between implants.

The healthy pelvis is analysed without implant, with a standard implant and with a custom-triflange implant.

3.2.1: Development of the FE components

A pelvis with an average shape was taken from the available samples. The first step was to ream the acetabulum by means of a virutal surgery. This was done in order to mimic the reality, where a portion of the cortical bone in the acetabulum is removed during preparation for the implant. This can have a significant effect on the stress-distribution. A approach was followed where boolean operations between a sphere and the pelvis (substraction of the sphere from the pelvis) were performed. Reaming was sequentially increased by 1mm untill the cancellous bone was visible [36] [37].

A standard hemispherical cup was modelled with a diameter equivalent to the final reaming size (58mm) and with a thickness of 4mm [38]. The custom triflange implant was modelled by adding 3 customized flanges to this cup in 3Matic (Materialise Leuven, Belgium). Models with added liner and femoral head were also developed, to study the effect of these components. The liner was modelled as a hemisphere with an outside diameter equivalent to the inner diameter of the cup and with a thickness of 6mm [39]. The femoral head was then modelled as a sphere flattened on one side, with a diameter equivalent the the inner diameter of the liner.

3.2.2: Material parameters

Components of the implant were modelled with homogeneous, linear-elastic and isotropic material properties. The bone of the pelvis was modelled as heterogeneous, linear-elastic and isotropic. The Young's-modulus for cortical bone ($E > 13028$) is defined as [40]:

$$E = 23440 * (1-p)^{5.74} \tag{6}$$

In addition, this relation can be formed for cancellous bone ($E < 13028$) [40]:

$$E = 14927 * (1-p)^{1.33} \tag{7}$$

Here, p represents the porosity of bone (a value between 0 and 1) and E represents the Young's modulus in Mpa. This porosity is defined as [41]:

$$p = \frac{BMD - BMD_{max}}{Pv - BMD_{max}} \tag{8}$$

Here, p represents the bone-porosity (between 0 and 1), ***BMD*** is the bone mineral density (g/cm^3), ***BMD$_{max}$*** is the maximum bone mineral density (g/cm^3) and ***Pv*** is the density of the voids (g/cm^3). The chosen value for ***Pv*** is 0. The remaining variables are defined as [42]:

$$BMD = 0.001 * HU \tag{9}$$

$$BMD_{max} = 0.001 * HU_{max} \tag{10}$$

Here, HU and HU_{max} represent the measured Hounsfield Unit for each pixel and the maximum Hounsfield unit measured in the CT-scan respectively. These values can be determined directly from Mimics.

Material constants for the cup were derived by taking the average of multiple values reported in literature [43, 44, 45, 46, 47, 48, 49, 50, 51]. The same was done for the liner [43, 52, 53, 54, 55, 56, 57] and the femoral head [55, 56]. Computed values can be seen in table 1.

3.2.3: External loads

To study the stress distribution in the pelvis, three loading scenarios were included in the model. To be able to predict bone remodelling in an accurate manner, it is necessary to include both high-magnitude forces with a low frequency and low-magnitude forces with a high frequency

Table 1: Material properties of the Finitie Element-components

Component	Material used	Youngs Modulus (Mpa)	Possion's ratio [-]	Density (g/cm^3)
Cup	Titanium	110,000	0.3	4.43
Liner	UHMWPE	1,200	0.4	0.93
Femur	Cobalt-chrome	420,000	0.3	8.5
Pelvis	Bone	Based on uquation	0.3	Based on equation

[47].With this in mind, the chosen loading scenarios included walking, stair-climbing and stumbling. To implement a bone remodelling-algorithm, it is therefore necessary to determine both the magnitude and the frequency of each load. For the walking scenario, the magnitude is based on a low-magnitude force occurring during the walking cycle, which is measured with instrumented implants [58]. The same is done for stair-climbing and stumbling [59]. The amount of cycles for each loading scenario is adapted from literature [60]. The magnitude and frequency of each scenario can be seen in table 2. Forces were applied to the acetabulum as a evenly distributed static pressure, with the direction orthogonal to the surface. For the cases with implants, the load was applied in the same manner, except the load was applied to the titanium cup. The chosen surface for the pressure consisted out of the area which was in contact with the femoral head for load transmission. This contact area was different for each scenario. An estimation of the contact area for each scenario was made based on literature [61]. The chosen areas can be seen in figure 7.

In addition to the hip contact forces, muscle forces were also included in the model. It was evident that without muscle forces the predicted BMD's after bone remodelling were too high, as a result of absence of strain in certain areas. Therefore 20 muscle forces were included in the bone-remodelling model, as can be seen in table 3. The magnitude of muscle forces during walking were taken from literature [63]. The direction and attachment site of each muscle was determined by studying the muscle fiber direction and attachment area at Biodigital [62], as can be seen in figure 8. Since limited data on muscle forces during stair-climbing and stumbling was available, it was assumed that the muscle-forces increased respectively with a factor 3 and 8 with respect to walking-scenario. This assumption was made based on the somewhat similair scale for the acetabular forces occuring during the different scenarios. It should be noted that muscle forces are only included in the bone-remodelling model and not in the single-load cases.

Table 2: Magnitude and frequency of forces for each loading scenario

Scenario	Magnitude of force (N)	Frequency (cycles/day)
Walking	625	3000
Stair-climbing	1876	112
Stumbling	5000	1

Table 3: Magnitude of muscle forces during walking. Magnitudes of the resulting and directional forces are shown, both for the total muscle force and the muscle force per node.

Muscle	Muscle force total and per node	Total force split-up in 3 directions	Node force split-up in 3 directions
Gluteus medius	Total: 600N 189 nodes 3.16N/node	x: 424 N y: 0 N z: -424 N	x: 2.2 N y: 0 N z: -2.2 N
Gluteus minimus	Total: 60N 30 nodes 2N/node	x: 42 N y: 0 N z: -42 N	x: 1.4 N y: 0 N z: -1.4 N
Tensor fascia latea	Total: 150N 25 nodes 6N/node	x: 60 N y: 60 N z: -125 N	x: 2.4 N y: 2.4 N z: -5 N
Iliacus	Total: 300N 121 nodes 2.4N/node	x: -150 N y: -150 N z: -125 N	x: -1.2 N y: -1.2 N z: -1.8 N
Psoas minor	Total: 300N 52 nodes 6N/node	x: 0 N y: -120 N z: 280 N	x: 0 N y: -2.4 N z: 5.6 N
Gracilis	Total: 150N 52 nodes 3N/node	x: 0 N y: 32 N z: -160 N	x: 0 N y: 0.6 N z: -3 N
Sartorius	Total: 150N 37 nodes 4N/node	x: -75 N y: -30 N z: -127.6 N	x: -2 N y: -0.8 N z: -3.4 N
Semi-membranosus	Total: 60N 189 nodes 3.2N/node	x: 42 N y: 0 N z: -42 N	x: 1.4 N y: 0 N z: -1.4N
Semi-tendinosus	Total: 400N 75 nodes 5.2N/node	x: 0 N y: 0 N z: -400 N	x: 0 N y: 0 N z: -5.2 N
Biceps femoris longus	Total: 200N 36 nodes 5.6N/node	x: 0 N y: 0 N z: -200 N	x: 0 N y: 0 N z: -5.6 N
Adductor longus	Total: 150N 49 nodes 3N/node	x: 0 N y: -40 N z: -150 N	x: 0 N y: -0.8 N z: 3 N
Adductor magnus	Total:250N 84 nodes 3N/node	x:0 N y: 0 N z: -250 N	x: 0 N y: 0 N z: -3 N
Adductor brevis	Total: 200N 35 nodes 6N/node	x: 0 N y: 140 N z: -140 N	x: 0 N y: 4.2 N z: -4.2 N
Obturator externus	Total: 200N 109 nodes 2N/node	x: 42 N y: 0 N z: -42 N	x: 1.4 N y: 1.4 N z: 0 N
Pectineus	Total: 200N 78 nodes 2.6N/node	x: 138 N y: 0 N z: -132 N	x: 1.8 N y: 0 N z: -2 N
Obturator internus	Total: 150N 70 nodes 2N/node	x: 100 N y: 100 N z: 0 N	x: 1 N y: 1 N z: 0 N
Quadratus femoris	Total: 200N 51 nodes 4N/node	x: 200 N y: 0 N z: 0 N	x: 4 N y: 0 N z: 0 N
Superior gemellus	Total: 150N 31 nodes 6N/node	x: 150 N y: 0 N z: 0 N	x: 6 N y: 0 N z: 0 N
Inferior gemellus	Total: 150N 31 nodes 6N/node	x: 150 N y: 0 N z: 0 N	x: 6 N y: 0 N z: 0 N
Rectus femoris	Total: 200N 40 nodes 5N/node	x: 0 N y: 0 N z: -200 N	x: 0 N y: 0 N z: -5 N

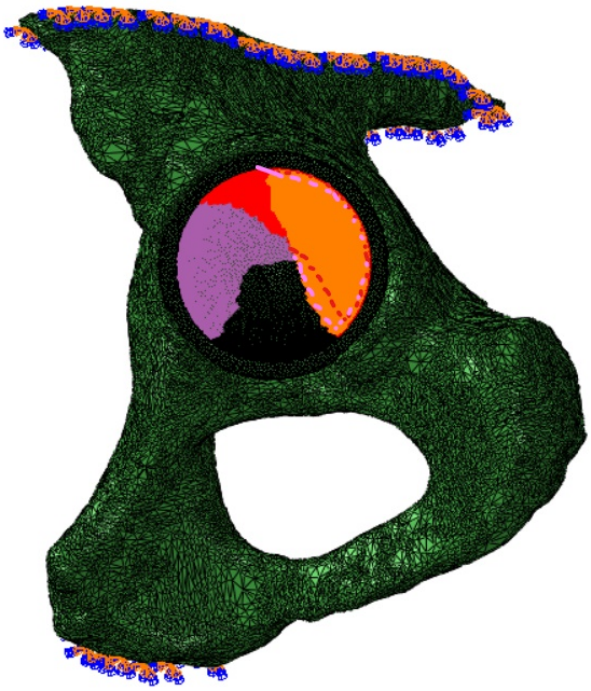

Figure 7: The area of the applied pressure in the acetabulum. Purple = area for walking, Red = area for stair-climbing and Orange = area for stumbling

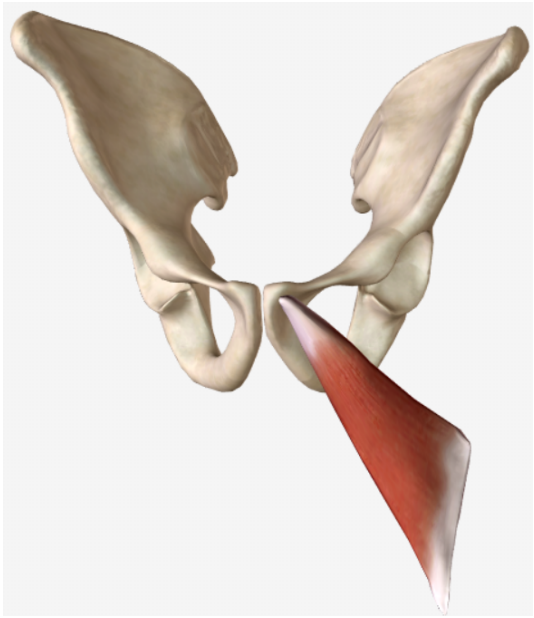

Figure 8: Anatomy study to determine the muscle fiber direction and attachment area. Images used from biodigital [62]

3.2.4: Meshing the model

To determine the optimal amount of elements for the model, multiple iterations were performed by changing the element size, with the objective to minimize the amount of distorted elements. Due to the fact that the material properties of the pelvis depended on the Houndsfield-unit, the pelvis had to be meshed in 3-Matic and exported as an orphan-mesh to Abaqus. This allowed only the use of tet4 and tet10 elements, which are first-order tetahedral elements. It is shown that for these type of simulations, it is better to use hexagonal elements in combination with a quadratic formulation, to prevent locking [64]. Since changing the element type was not an option, the mesh of the pelvis was refined. Although it is more effective to increase the order of the mesh rather than refining the mesh [64], it was found that with the refined mesh it was possible to obtain accurate results.

Both the standard hemispherical cup and the triflange cup were meshed in the same manner as the pelvis. The mesh for these components was even finer, which is a requirement for the master-slave interface between the pelvis and the implant, as highlighted in the next section. An overview of the amount of nodes and elements for each component is given in table 4. From the 125.592 elements on the pelvis, 6858 (5,5%) were distorted. In total, the FE-model consisted out of 644.172 elements and 669.577 nodes.

Table 4: Mesh-attributes of the FE-model

Component	**Type of elements**	**Amount of elements**	**Amount of nodes**
Pelvis	C3D4 (first-order tet)	125.592	33.360
Hemispherical cup	C3D4 (first-order tet)	248.134	45.679
Triflange cup	C3D4 (first-order tet)	64.328	19.824
Liner	C310M (quadratic tet)	115.059	170.641
Femoral head	C310M (quadratic tet)	91.059	400.073
Total	-	644.172	669.577

3.2.5: Boundary and interface conditions

To fix the model in 3D-space, boundary conditions are required that prevent translation and rotation. To mimic the reality, two boundary conditions were applied to the pelvis, which both use the encastre formulation (U1 = U2 = U3 = UR1 = UR2 = UR3 = 0), which prevent rotation and translation in every direction. The first boundary condition acted on the pubic symphysis, while the second acted on the cutting area near the sacroiliac joint [52].

In addition to the fixation of the pelvis, interface conditions need to be defined between the components of the model. Three interfaces can be indetified, namely:

- The bone-implant interface
- The implant-liner interface
- The liner-femoral head interface

Two scenarios were evaluated, one case with all interfaces glued [43] together and one case where all interfaces are node-tyed [56]. This is done in order to determine which scenario gives a more realistic result.

3.3: Development of the Finite Element Model for the defect pelvis

A FE-model of a defect pelvis was developed to study the potential of a deformable implant. First, a 3D model was evaluated with an implant which had the exact shape of the defect, to study the stress-shielding effects compared to the triflange-implant. This was done by the use of the bone-remodelling algorithms. Next, a 2D model was built to determine if it is achievable to acquire this level of deformation with the deformable implant.

3.3.1: Development of the FE components

The defect pelvis was acquired by taking the average healthy pelvis and applying the defects from the statistical shape model of the defect pelvis. The stress-shielding of this defect pelvis was determined with both the triflange and the deformed implant by using the bone-remodelling algoritms. Both implants were developed with computer-aided design. The defect pelvis with the defect-shaped implant can be seen in figure 9.

Figure 9: The damaged pelvis and the defect-shaped implant

Next, to determine if this amount of deformation can be acquired with the deformable cup, several deformable acetabular cups were developed, which were pressed into multiple damaged pelvises. The deformable cup was modelled as a 2mm solid titanium layer on the inside with a unit cell structure-layer on the outside (rhombic dodecahedron unit-cells with 90% porosity). To reduce computational power, this unite-cell structure was modelled as a solid section with material properties of the unit-cell (figure 10). The interference fit (the difference in radius between the acetabulum and the acetabular cup) and the thickness of the unit-cell layer were varied. Cups with a thickness of 9, 12 and 15mm and a interference-fit of 0,1,2 and 3mm were evaluated. Combining these parameters resulted in 12 different designs for the deformable cup. These cups were pressed into pelvises with different types of defects. The procedure of pressing the cups inwards was performed by an undeformable hammer.

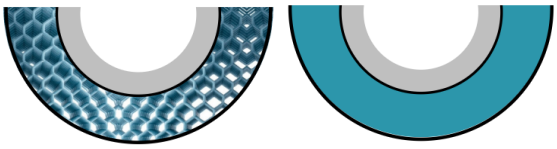

Figure 10: The actual implant design for the deformable cup (left) and the simplification (right). Grey displays the stiff titanium and blue the porous deformable part.

The parameters in the next sections describe the properties of the deformable cup-model. The model-parameters of the defect-shaped implant are identical to the model-properties of the healthy pelvis.

3.3.2: Material parameters

For the model with the deformable cup, the solid layer was modelled as titanium (table 1). The rhombic dodecahedron unit-cell layer material-properties were based on experimental results (figure 11), which defined both elasticity (E=114 Mpa) and plasticity. The Poisson's ratio from the experimental results was higher than the theoretical value of 0.45/0.5, due to the printing process. In the FE-model, this maximum theoretical value was used nevertheless.

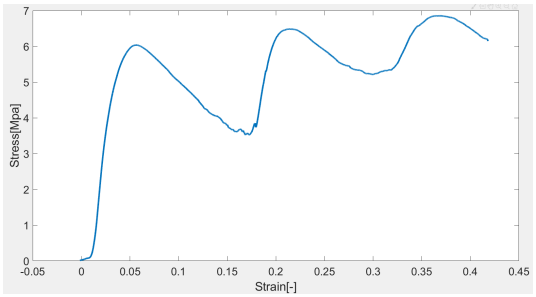

Figure 11: Experimental material properties for the porous structure

3.3.3: External loads

The deformable cups were pressed into the acetabulum based on four displacement-based loads. The amount of displacement increased with each load, resulting in displacements of 9, 10, 11 and 12mm. This approach is similar to the procedure for pressing in standard hemispherical

cups (figure12 [65]). Note that in this study increased displacement is used instead of increasing force.

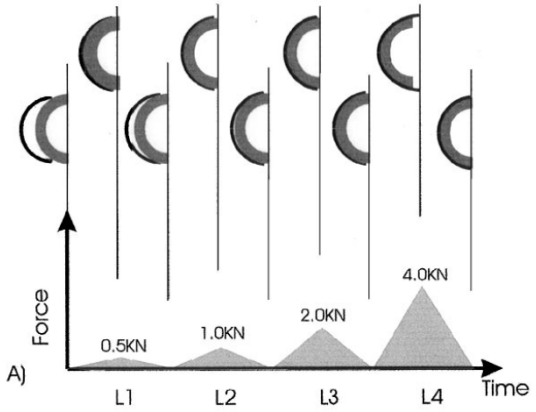

Figure 12: Four increasing loads are used to hammer the acetabular cup into the pelvis [65]

3.3.4: Meshing the model

The components are meshed with 2D-elements. The specification and amount of elements for each components are displayed in table 5.

Table 5: Mesh-attributes of the deformable cup FE-model

Component	Type of elements	Amount of elements	Amount of nodes
Pelvis	R2D2 (Linear-line)	222	224
Deformable cup	CPS4R (quad-rilateral)	7.772	8.070
Hammer	R2D2 (Linear-line)	333	332
Total	-	8.327	8.626

3.3.5: Boundary and interface conditions

The pelvis was fixated on the whole outer surface, which prevented movement in all directions. The same boundary condition applied to the hammer, except that movement in the y-direction was allowed. The cup was unconstrained and was free to move in all direction. However, a friction-based interaction property was defined between the cup and the pelvis, with a friction coefficient of μ = 0.3.

3.3.6: Performance evaluation

To asses the feasibility of the deformable cup, four variables are measured for each design, namely:

- **The gap distance, Gd**: The remaining distance between the deformed cup and the pelvis after the 4th loading cycle measures how well the implant is deformed into the defect.
- **The pull-out force, Fo**: The force required to pull the implant out of the acetabulum is an indication of the implant stability.
- **The stress at the bone-interface, Sb**: The stress at the acetabulum should be minimized in order to prevent further bone damage.
- **The push-in force, Fi**: The force required to push the implant in the acetabulum. It is desired to keep this as low as possible to allow convenient surgery.

Based on these parameters, a performance function can be constructed. It can be seen that all above-mentioned variables should be minimized, except for **Fo**. This performance function can then be formulated as:

$$P = a*(1-Gd)+b*Fo+c*(1-Sb)+d*(1-Fi) \quad (11)$$

Here, Gd, Fo, Sb and Fi are the above-described parameters, divided by the maximum value found, resulting in values between 0 and 1. The parameters a, b, c and d are relative weighting scores, equal to 0.4, 0.3, 0.2 and 0.1 respectively. This results in a performance P, which can take values between 0 (poor) and 1 (excellent).

Finally, the damaged pelvises are categorized based on the size and shape of the defects. A machine learning algorithm is trained that can predict which deformable cup is most suitable for each pelvis, based on the defects. A Nearest neighbour predictor is used with the amount of neighbours n=1. The defect pelvises are classified based on the largest depth (D)/Length (L) ratio of the defect and the horizontal overlay (O_h), see figure 13. The horizontal overlay is defined as the summed gap depth in the horizontal direction, which prevents the cup from springing back after deformation. The training and test set size for the machine-learning algorithm is 18 and 3 respectively.

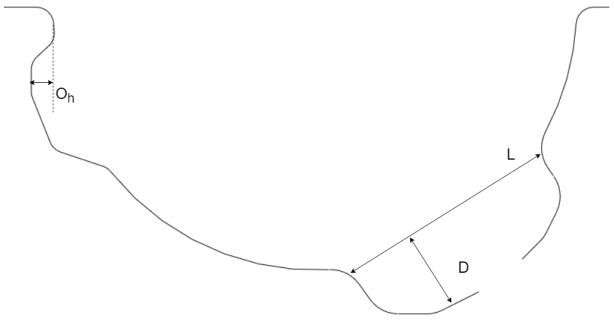

Figure 13: Classification of bone defects

3.4: The development of the bone-adaptation model

To predict the amount of stress-shielding with the different implant-designs, two bone-remodelling algorithms are implemented. The algorithms adapt the Young's modulus of the pelvis based on the strain in each element.

3.4.1: Implementation of the bone-adaptions models

Since the bone-remodelling algorithms adapt the Young's modulus, while the objective is to derive the BMD, a relation between these variables is needed. For this, the equations as specified in the material parameters section are used. Combining these equations and filling in the parameters gives the final relation between Young's modulus and BMD for cortical bone ($E > 13028$):

$$BMD = 0.8 + \frac{E^{(\frac{1}{5.74})}}{23440^{(\frac{1}{5.74})}} * -0.8 \qquad (12)$$

and for cancellous bone ($E < 13028$):

$$BMD = 0.8 + \frac{E^{(\frac{1}{1.33})}}{14927^{(\frac{1}{1.33})}} * -0.8 \qquad (13)$$

Here, E represents the Young's modulus (Mpa) and BMD the bone-mineral-density (g/cm^3). In this study two bone-remodelling algorithms are implemented, each with a different concept. The first model (model A) utilizes a relatively simple concept.The equations of this model are adapted from literature [66]. A stimulus signal (w) is defined as a function of strain and loading rate (lr, amount of loading cycles per day (frequency)):

$$w = rl * strain^m \qquad (14)$$

Here, m is a variable determining the relative weighting between loading rate and strain. The total stimulus signal is determined by summing the stimulus signals from every load case (walking, stumbling and stair-climbing). If the stimulus signal is higher than the equilibrium-stimulus, the Young's-modulus increases linearly. This continues until a Youngs-modulus is reached which produces a stimulus signal equal to the equilibirum-stimulus and a steady-state is reached (i.e. the stimulus signal lies within the "deadzone"). The opposite occurs when the stimulus signal is lower than the equilibrium stimulus. This concept is shown in figure 14. An overview of the model can be seen in figure 15, with parameter values shown in table 6. The model is implemented in FORTRAN as an UMAT-subroutine (User-Defined-Material-Model) which is then linked to Abaqus. The UMAT-subroutine of model A can be found in appendix B.

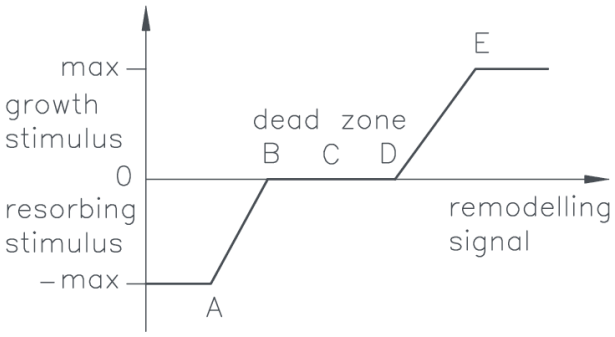

Figure 14: Concept of the first bone remodelling algorithm (model A). Image adapted from literature [67]

Table 6: Parameters used in bone-remodelling model A

Parameter	Symbol	Value
Loading rate stair-climbing	rl1	300
Loading rate stumbling	rl2	1
Loading rate walking	rl3	3000
Relative strain weight	m	4 [66]
Time-step (effects value of B)	dt	8
Remodelling coefficient (1 day) Remodelling coefficient (8 days)	B B	50.000 [66] 400.000
Width of lazy zone (one-sided)	s	0.00025
Equilibirum stimulus	wzero	0.0025

The second bone-remodelling model (model B) relies on a more complex principle which involves additional remodelling processes compared to model A. The equations for model B are adapted from literature [68]. Just like model A, model B also decreases the Young's modulus when the strain stimulus is below an equilibrium stimulus. However, there are two major differences between the models, namely:

- **Damage:** Whereas model A shows an increase in Young's modulus when the stimulus signal is far above the equilibirum stimulus, model B introduces a decrease in Young's modulus due to damage. This damage-induced decrease in Young's modulus increases proportionally with the difference between the stimulus and the equilibrium stimulus.
- **Activation frequency:** The stimulus signal in model B is also dependent on the strain. However, also other factors effect the stimulus signal, namely the amount of bone-resorbing/bone-refilling cells and the amount of bone which is formed/absorbed per cell. These factors in turn depend on the strain and which phase of the remodelling cycle is currently active (refilling/resorbing/reversal phase). Therefore, model B mimics the underlying principle of the bone.

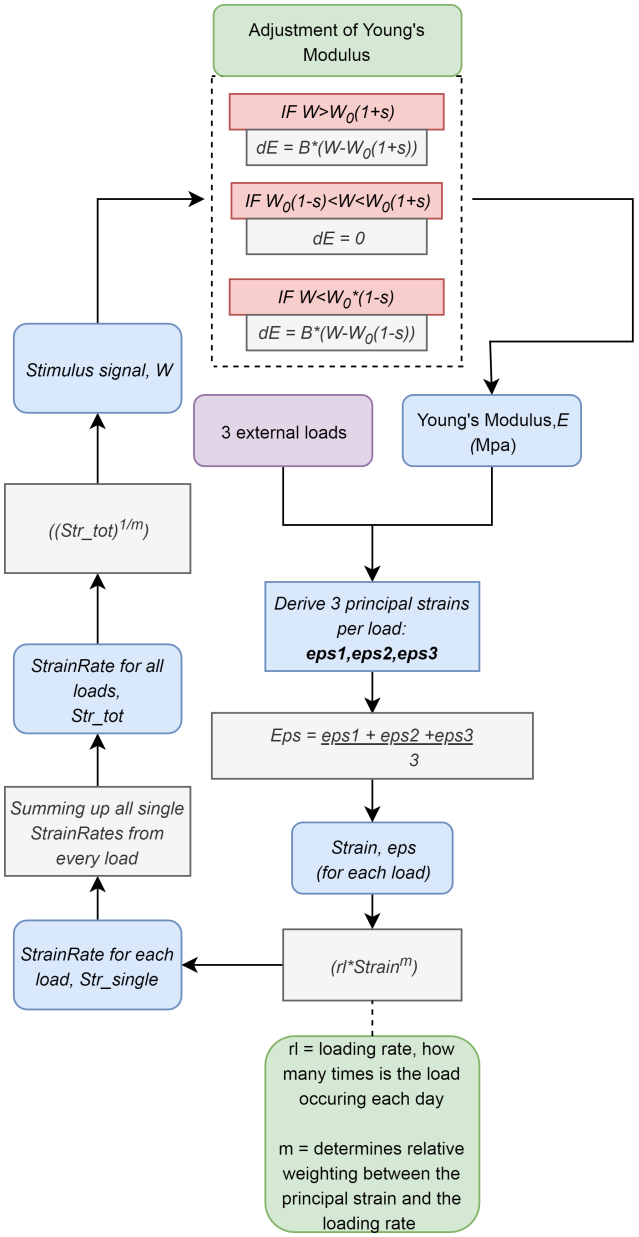

Figure 15: Bone remodelling model A

although several changes where necessary due to different subjects and environments. Loading rates were changed in order to mimic the chosen loading scenarios. Additionally, a time increment of 8 days was chosen to minimize simulation time. The equilibrium-stimulus was determined by trial and error.

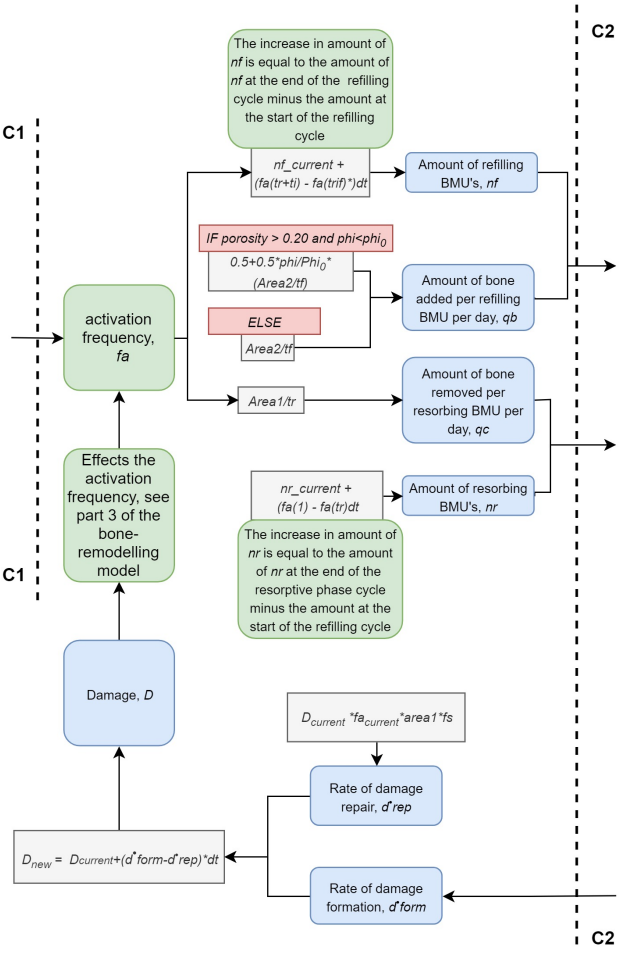

Figure 16: Bone remodelling model B, part 1: The remodelling section

An overview of model B can be seen in figure 16, 17 and 18. Due to complexity the overview is split-up in 3 images. C1 and C2 show the cuts of the model, i.e. the regions where the separate images are connected to each other. Again, a FORTRAN subroutine was written and implemented in the Abaqus model by linking. The FORTRAN file of model B can be found in appendix C. The parameter values of model B can be seen in table 7, 8 and 9. Table 7 shows the state variables (which change every iteration/step), table 8 shows constant variables, which remain unchanged in every step and table 9 shows variables which directly on the Young's modulus. Parameter values were adapted from literature [68],

Both models are evaluated to give insight in the performance of bone-density prediction models and to see what the advantages/disadvantages are of using a complex model over a relatively simple model. In addition, model B is included since it takes into account a damage factor. It is expected that implants will not only result in areas which are insufficiently loaded, but also in areas which will experience higher loads than without implants, due to the uneven stress distribution. By taking the damage factor into account, this decrease in Young's modulus due to high loading-patterns can be studied.

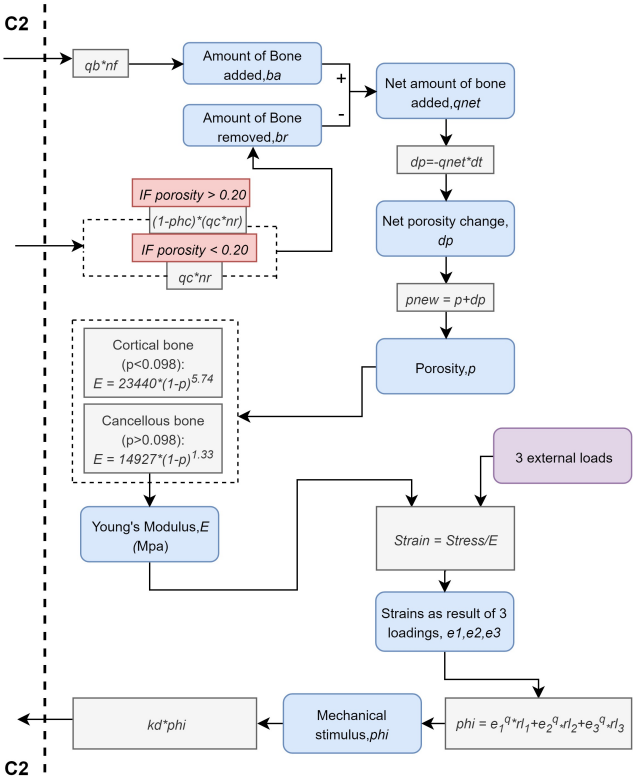

Figure 17: Bone remodelling model B, part 2: The removal and addition of bone

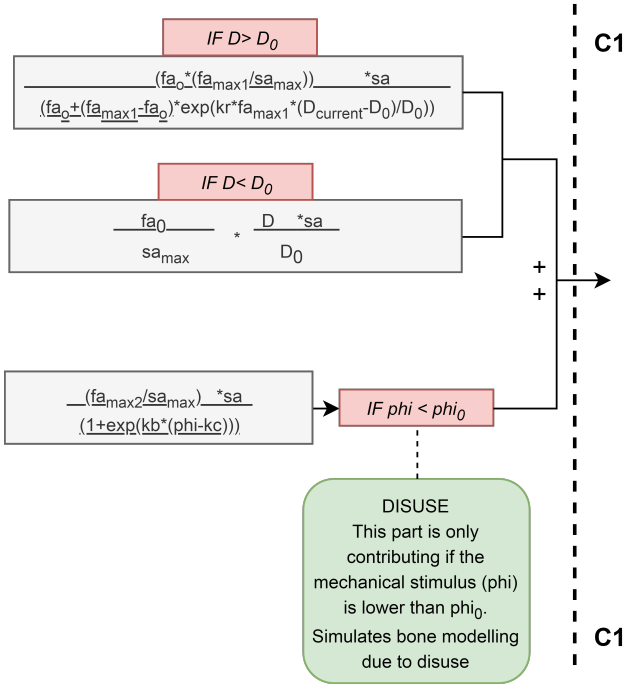

Figure 18: Bone remodelling model B, part 3: The activation frequency is calculated

Table 7: State variables of model B, which change every step

Parameter	Symbol	Initial value
Porosity	p	0.044321 [-]
Strain during stair-climbing	e_1	0 [-]
Strain during stumbling	e_2	0 [-]
Strain during walking	e_3	0 [-]
Mechanical stimulus	*Phi*	0 [strain/day]
Damage	D	0.366 [mm/mm^2]
Amount of bone-forming cells	*nf*	fa_0*tf [-]
Amount of bone-removing cells	*nr*	fa_0*tr [-]
Activation frequency	*fa*	0.00670 [BMU/ mm^2 /day]
Activation frequency of the past days	*fa-past*	-

Table 8: Constant parameters of model B, do not change each step

Parameter	Symbol	Value
Loading-rate stair-climbing	*rl1*	300 [-]
Loading-rate stumbling	*rl2*	1 [-]
Loading-rate walking	*rl3*	3000 [-]
Damage removal specifity factor	*fs*	5 [-]
Time step	*dt*	8 [days/step]
Maximum activation frequency	*famax1*	0.50 [BMU/mm^2 /day]
Maximum activation frequency for disuse	*famax2*	1.15 [BMU/mm^2 /day]
Maximum specific surface area	*samax*	4.1905 [-]
Activation frequency at equilibrium	*fa0*	0.00670 [BMU/mm^2 /day]
Radius for area calculation	*rc*	0.095 [mm]
Radius for area calculation	*rh*	0.020 [mm]
Damage rate exponent	*q*	4 [-]
Damage in equilibirum	*D0*	0.0366294 [mm/mm^2]
Damage rate coefficient	*Kd*	1088 [mm/mm^2]
Activation frequency dose-response coefficient	*Kr*	-1.6 [-]
Activation frequency dose-response coefficient	*Kb*	65E^9 [-]
Activation frequency dose-response coefficient	*Kc*	16E-9 [-]
Duration of resorptive phase of the remodelling cycle	*tr*	3 [days]
Duration of reversal phase of the remodelling cycle	*ti*	1 [days]
Duration of refilling phase of the remodelling cycle	*tf*	8 [days]
Total time of the remodelling cycle	*trif*	12 [days]
Equilibirum stimulus	*Phi0*	32E-9 [-]
Initial porosity	*Phc*	0.04432 [-]

Table 9: Parameters of model B which depend on the Young's modulus/porosity

Dependent variable	Symbol	Value
Young's modulus	E	- depends on E, see overview-
Specific surface area	Sa	*Sa = ((((28.8*p-101)*p+134) *p-93.9)*p+32.3)*p [-]*
Area for bone-formation/absorption	Area1	$Area1 = \pi * rh^2 IFp<0.20$ $Area1 = 0.5 * \pi * rc^2 IFp>0.20$
Area for bone-formation/absorption	Area2	$Area2 = \pi * (rc^2 - rh^2) IFp<0.20$ $Area2 = 0.5 * \pi * rc^2 IFp>0.20$

4.1.2: Modification of bone-remodelling model B

Model B utilises a remodelling algorithm which mimics the complex underlying principle of bone. However, the properties of each element are only determined by the stimulus signal for that particular element. It is expected that bone properties are influenced by multiple sensors (osteocytes), where sensors that are closer contribute more than sensors which are far away [69]. To implement this in the model, the stimulus signal of the surrounding elements are taken into account. The amount of surrounding elements that contribute is determined by k1 and k2 for a 2D example (figure 19).

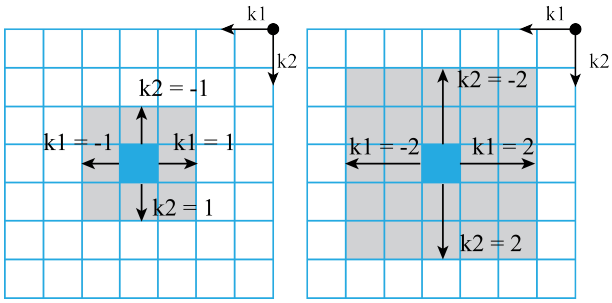

Figure 19: The stimulus signals (grey) that contribute to the adaptation of the blue element is determined by the k-values

In 3D, the scenario can be expanded with one extra parameter, k3. In this study, k1, k2 and k3 are identical, to obtain a square surrounding box. Once the contributing elements have been selected (by choosing k1,k2 and k3), the amount of contribution of each element is determined by following an exponentially decaying function with increasing distance [70]. This amount of contribution can be calculated with:

$$C_i(x) = e^{-d(x)/D} \tag{15}$$

Here, C represents the contribution of element i to a certain location x, d is the distance between the element and this location and D determines the rate of spatial decay.

The distance between each element and the location is measured as the euclidean distance:

$$d(x) = \sqrt{k1^2 + k2^2} \tag{16}$$

It should be noted that with a finer mesh, the actual distance (in mm) decreases if the k-values remain constant, since k1 and k2 are defined in terms of amount of elements. To account for this effect, the k-values are scaled with a factor which depends on the mesh refinement.

In theory, the rate of spatial decay could be chosen in such a way that all elements will contribute to a certain location, with the elements the furthest away contributing for a very small negligible amount. However, including all elements for every location will result in larger computational time, since every stimulus signal will consist out of thousands of values. Looping over all of these values results in longer simulations and is not preferred. Therefore, the approach of selecting elements with k1, k2 and k3 is combined with the equation of spatial decay: The amount of elements that are contributing are determined based on the k-values. Of these contributing elements, the equation of spatial decay is applied. Note that this is only done for bone-remodelling model B. For model A, the change in properties is only determined by the stimulus signal of that particular element. This is done in order to keep model A relatively simple, to allow studying the differences between a simple and complex bone-remodelling model. The optimal values of k are determined during the validation step, as highlighted in the next section.

4.1.3: Validation of the bone-remodelling models

In order to determine how well the models predict the BMD-values of the bone, two validation steps are performed: (1) Comparing model-predictions with real values (from Mimics) and (2) comparing model-results with other bone-remodelling models from literature.

For the first validation, real BMD-values from the pelvis are extracted from Mimics at multiple locations. BMD-values are calculated by using the Houndsfield Unit from Mimics [40]:

$$P_{app} = 0.001 * HU \tag{17}$$

Here, *HU* represents the grey-value which can be obtained from Mimics. To obtain the BMD-values of the model, a homogeneous initial Young's modulus of 18070 Mpa is applied to the pelvic FE-model without implant. The bone-remodelling algorithm is run until a steady-state has been reached, i.e. the change in BMD is less than 0.05 over a time-span of 20 days. Then, the BMD-values of the model and the real values are compared and an error-function can be defined:

$$Err = \sum_{i=1}^{n} |BMD_{real} - BMD_{pred}| \tag{18}$$

Here, *Err* is the total error between the model prediction and the actual values, i is the element number and BMD_{pred} and BMD_{real} are the predicted and real BMD-values of the pelvic bone respectively. The objective is to

minimize this error function. This is done by running multiple bone remodelling simulations with different values for the equilibrium stimulus. By trial and error, the optimal value is then found.

The second validation consists of running the models on a simple 2D square. Then, the patterns are compared to a bone-remodelling model which is trained with neural networks with a forward approach [71]. This model has high correlations with the reality. Consequently, if in this study similair BMD-patterns are found, it is an indication of good performance. To do so, two types of loadings are used, which is similair to the method of the model from literature (figure 20). The magnitudes of the forces are identical aswell and are specified in table 10.

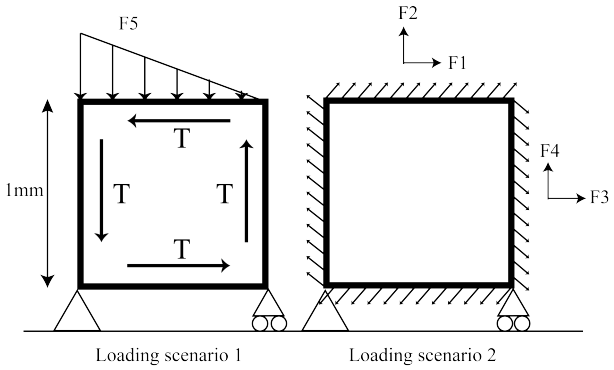

Figure 20: A simple 2D square is subjected to two loads and the BMD is altered with the bone-remodelling algoirthms

Table 10: Values for the forces during the second validation

	Fl	**F2**	**F3**	**F4**	**F5**	**T**
Force (N/mm^2)	4.8	4.6	2.4	3.0	10	3.5

The parameters of both models are varied and by trial and error the optimal values are found during these validation steps. These optimal values are then used in the other simulations.

4: Results

Results are split-up in 5 sections, namely:

- Results from the statistical shape model.
- Results of the healthy pelvis FE-model for the single-step load cases.
- Results of the validation of the bone-remodelling algorithms.
- Results of pelvis BMD-values with the standard, triflange and deformed implant after bone remodelling.
- Results of the deformable implant.

4.1: Results from the Statistical shape model (SSM)

This section displays the main modes of deviation for both the statistical shape model of the healthy pelvises and the defect pelvises. In addition, performance of the models is shown to asses the quality of the model-predictions.

4.1.1: The SSM of the healthy pelvises

For the healthy pelvises a total of 154 deviation-modes were found. However, the majority of these modes describe minor differences (such as small pits and bumps at the surface), which are not considered as a mode of interest. The modes were ranked from high to low, based on amount of deviation. The six main modes are considered here for analysis, which are displayed in figure 21. The first and third column show the pelvis shape for -3 and +3 times the standard deviation respectively (-3 SD and +3 SD). The column in between shows the mean shape of the pelvis. Red arrows describe the major differences between the 2 extreme shapes. In addition, the deformation-vectors are calculated for each mode and shown in the last column. These vectors are calculated by subtracting every cloud point of the -3 SD shape from the corresponding cloud point on the +3 SD shape. As a result, 2 points which are far apart (large deformation) result in a large vector. These vectors are then coloured based on size, where red shows the largest vectors.

The fist mode displays the deviation around the pubic symphysis and the pubic arch. The distance and shape between the obturator formamen and the pubic symphysis shows a notable deviation, together with the shape of the pubic symphysis itself. The second mode shows the inward pulling of the ilium-body, which in turn affects the anterior iliac spine and the greater sciatic notch. Mode 3 displays the deformation of the ischial tuberosity and spine. This mode can therefore affect the slenderness of the pelvis, giving either a more compact and short pelvis or a more slender and long pelvis. Mode 4 displays a somewhat similair effect for the ischial ramus. This area can be thin and tall or more bulky and short. For mode 5, the focus is on the anterior inferior spine. The long axis of this spine can point more towards the medial side or towards the lateral side. Next, mode 6 describes the deviation of the superior pubic ramus. The transition from the acetabulum can be more bulky or more smooth, which in turn affects the thickness of the acetabular rim.

Since the acetabulum is one of the focus-points of this study, the modes that describe the deviation at this area

are also included, see figure 22. It should be noted that these modes are mode 18,19 and 20. Therefore, the deviation described by these modes is minimal compared to the first six modes. The first mode of the acetabulum (mode 18) describes the deviation at the transition of the acetabular fossa and the lunate surface, towards the medial site. This transition can either be more towards the posterior site or towards the anterior site, affecting the relative size between the acetabular fossa and the lunate surface. Mode 19 describes an identical behaviour on the lateral side of the acetabular fossa. Next, mode 20 describes the thickness or difference in height between the lunate surface and the acetabular fossa.

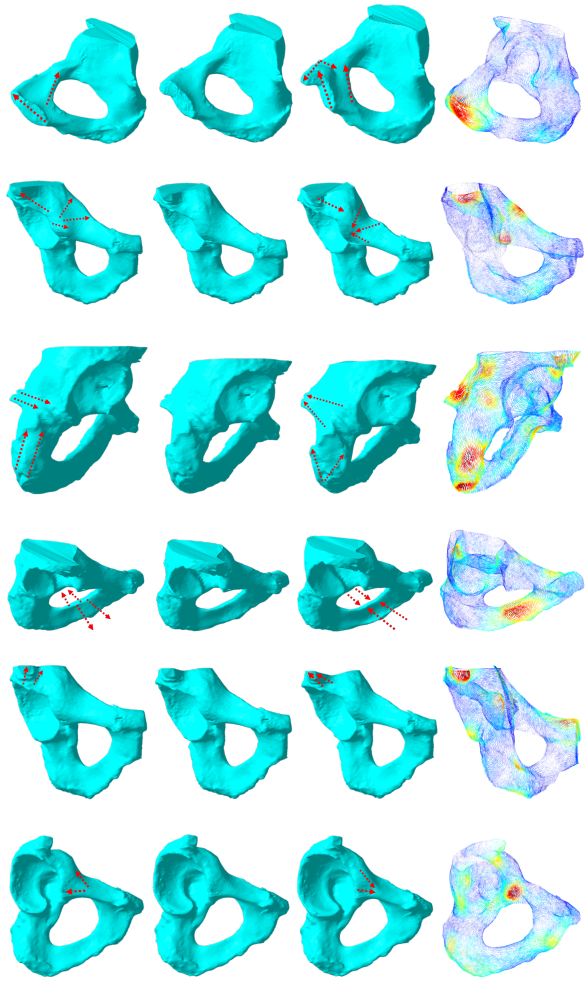

(a) -3 SD (b) Mean (c) +3 SD (d) Vectors

Figure 21: The six main modes of deformation for the healthy pelvises

4.1.2: The SSM of the defect pelvises

For the defect pelvises, a substantial amount of deviation was seen for the modes, see figure 23. It is expected that these results are not very accurate due to the limitation of

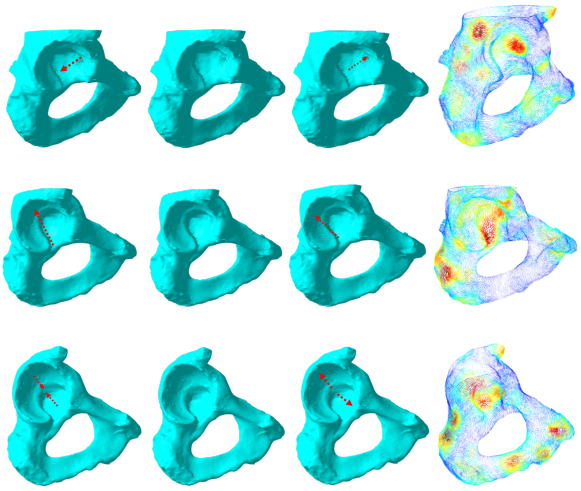

(a) -3 SD (b) Mean (c) +3 SD (d) Vectors

Figure 22: The modes of deformation at the acetabulum (mode 18,19 and 20)

samples, However, the relative deviation can give a general idea on the shape of the defect pelvises. The first mode describes the general orientation of the 2 defects in the acetabulum. These can either have a horizontal or vertical orientation. Mode 2 focuses on the inferior part of the actabulum, which can either lie along the horizontal line or can be tilted with an angle. Next, mode 3 describes the shape of the acetabular rim at the dorsal area, which can be either relatively straight or curved. Mode 4 represents the defect at the ischial ramus. A notch can be found in this area, resulting in a thinner ischial ramus which is pushed down a little. For mode 5, the anterior inferior spine can either have a slender shape or more bulky, which in turn affects the acetabular rim-thickness. The last mode (mode 6) describes the degree of the acetabulum which is pushed inwards. This in turn affects the disruption of the hemispherical shape of the acetabulum.

4.1.3: Performance results

The generalization ability of the SSM for the healthy pelvis is calculated with different amount of modes (figure 24). It can be seen that a higher amount of modes results in a lower error. This is due to the fact that with more modes the statistical model is able to represent the pelvis which was left out in a more accurate manner.

The model specificity, which measures the validity of the constructed shapes, increases with the amount of modes (figure 25a). The increase is relatively modest, but becomes more clear when averaging over neighbouring points (figure 25b). A higher amount of modes results in shapes which are deviating from the training shapes to a greater extent and thus less valid shapes.

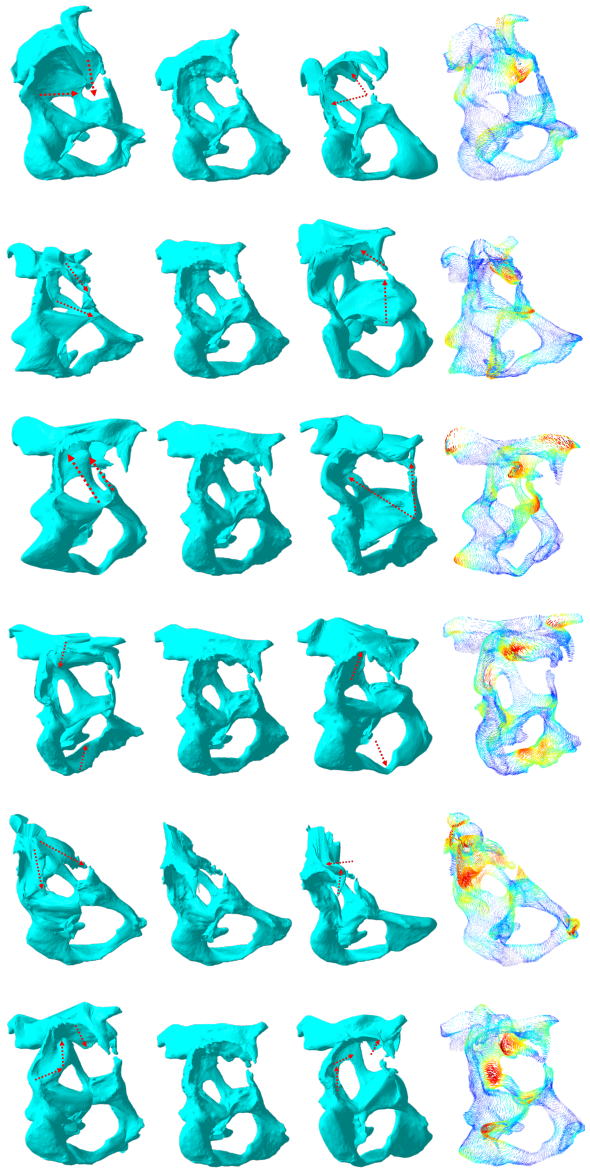

(a) -3 SD (b) Mean (c) +3 SD (d) Vectors

Figure 23: The six main modes of deformation for the defect pelvises

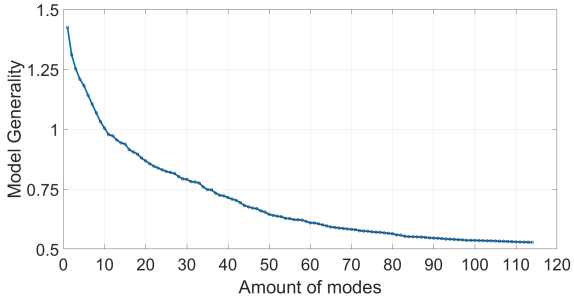

Figure 24: Generality of the SSM (healthy pelvis)

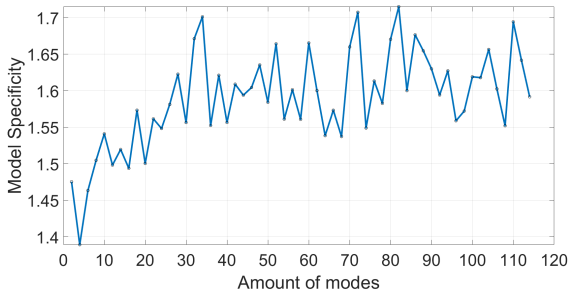

(a) Not averaged

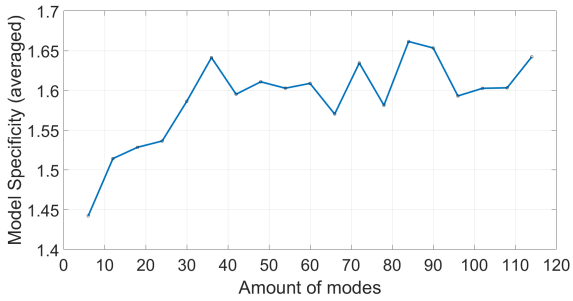

(b) Averaged

Figure 25: Specificity of the SSM (healthy pelvis)

4.2: Results of the Healthy pelvis FE-model for the single-step load cases

The results in this section display the stresses and strains after a single step, i.e. a static load is used for each scenario and the bone-remodelling algorithm is not applied here.

4.2.1: Pelvis without implant

The strains and stresses for each loading case of the pelvis without implant can be seen in figure 26. It can be seen that the stresses and strains increase linearly with the applied pressure, e.g. a pressure with a magnitude of twice as high results in stresses and strains twice as high. In addition, it becomes evident that during walking, the strains are relatively evenly distributed over the acetabulum. During stair-climbing and stumbling, a less evenly strain distributed can be noticed, causes by the non-uniform contact areas.

4.2.2: The standard cup

The FE-model of the standard cup was simulated with and without the liner and femoral head. It was found that these 2 components have a minimal effect on the stress/strain-distribution at the pelvis-cup area. In addition, it was found that the glueing-interface resulted in unrealistic high stresses, most likely caused by the distorted elements. These findings led to the decision to perform the simulations without the liner and femoral head and with node-tying as interface condition. Figure 27 shows the stresses and strains in

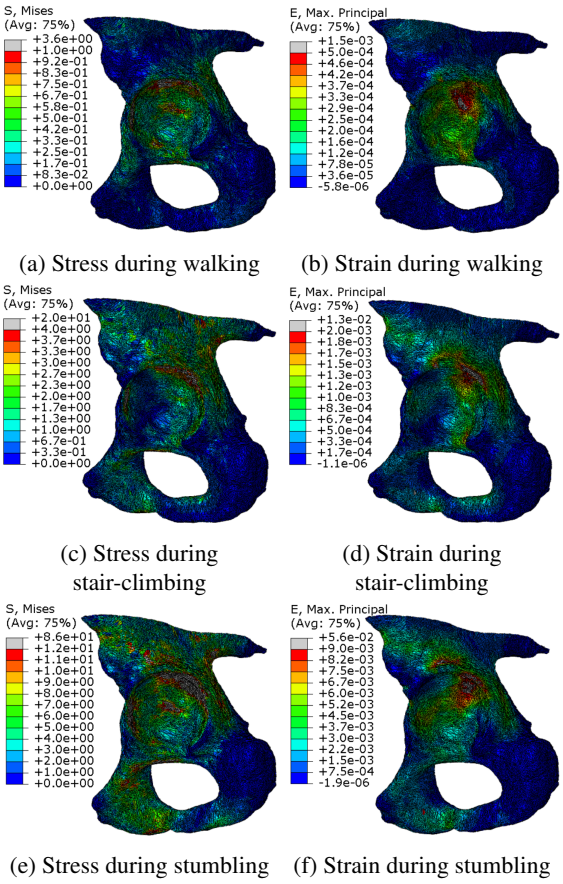

(a) Stress during walking (b) Strain during walking

(c) Stress during stair-climbing (d) Strain during stair-climbing

(e) Stress during stumbling (f) Strain during stumbling

Figure 26: Stresses and strains of the pelvis (without implant) during different loading cases

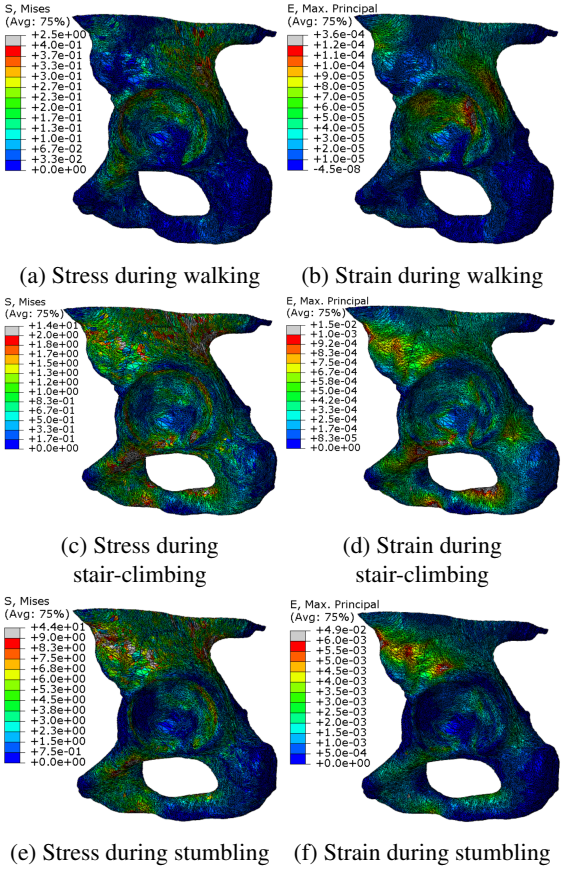

(a) Stress during walking (b) Strain during walking

(c) Stress during stair-climbing (d) Strain during stair-climbing

(e) Stress during stumbling (f) Strain during stumbling

Figure 27: Stresses and strains of the pelvis (with standard cup implant) during different loading cases

the pelvis (with standard cup implanted) during the three different loading scenario's. Figure 28 shows the corresponding results for the standard implant. The orientations of the cups are identical to their corresponding pelvises in figure 27. It can be seen that the strains in the pelvis have a lower magnitude than in the case without implant, indicating that the standard implant shows signs of stress-shielding. The amount of this effect can be determined by the bone-remodelling algorithm as shown in the next sections. However, it should be noted that the strain is still quite evenly distributed, comparable to the pelvis without implant. The stress and strain in the implant show a similair distribution as in the pelvis and remain far under the damage criterion for the material.

4.2.3: The triflange cup

Similar to the pelvis with standard implant, the pelvis with triflange implant was also modelled with and without the liner and femoral head, In addition, the 2 interface conditions (node-tying and glueing) were both evaluated. The same results regarding the effect of these additional components and the interface-options were found as in the case with the standard implant. Therefore, this led to the decision to perform the simulations without the liner and femoral head and with node-tying as interface condition. Figure 29 shows the stresses and strains in the pelvis (with triflange cup implanted) during the three different loading scenario's. Figure 30 shows the corresponding results for the triflange implant. The orientations of the cups are identical to their corresponding pelvises in figure 29.

Looking at the hemispherical part of the triflange implant, it can be seen that the strain/stress distribution is similair to the standard cup. The magnitude in this area is lower for the triflange implant, which is most likely caused by the additional flanges. High stress-concentrations are found at these flanges, in particular the most cranial flange. Analyzing the strains in the pelvis with triflange implant shows that the magnitudes are lower than the pelvis without implant and the pelvis with standard implant. Again, this is an indication that more stress-shielding occurs with the triflange implant compared to the situation without implant and the standard implant. In addition to the lower magnitude, it can be seen that the strain in the pelvis is less evenly distributed compared to the other two scenarios. This effect is most likely caused by the flanges, which alter the natural hemispherical shape of the acetabular area.

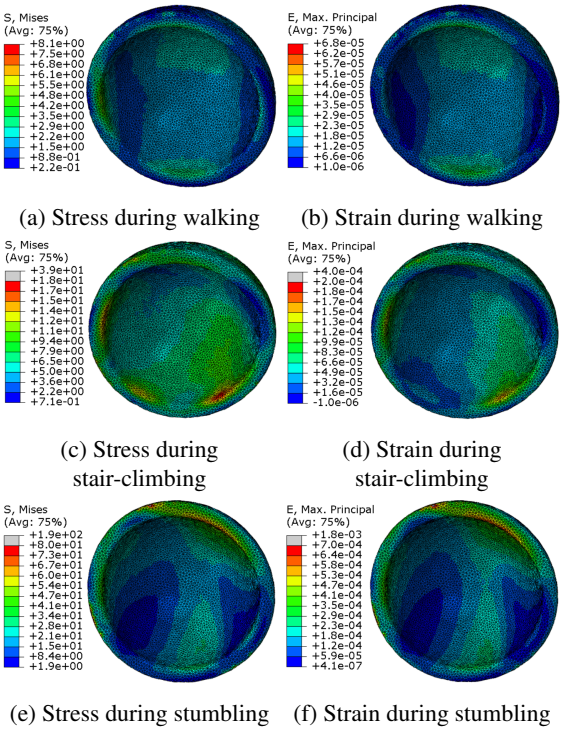

(a) Stress during walking (b) Strain during walking

(c) Stress during stair-climbing (d) Strain during stair-climbing

(e) Stress during stumbling (f) Strain during stumbling

Figure 28: Stresses and strains of the standard cup during different loading cases

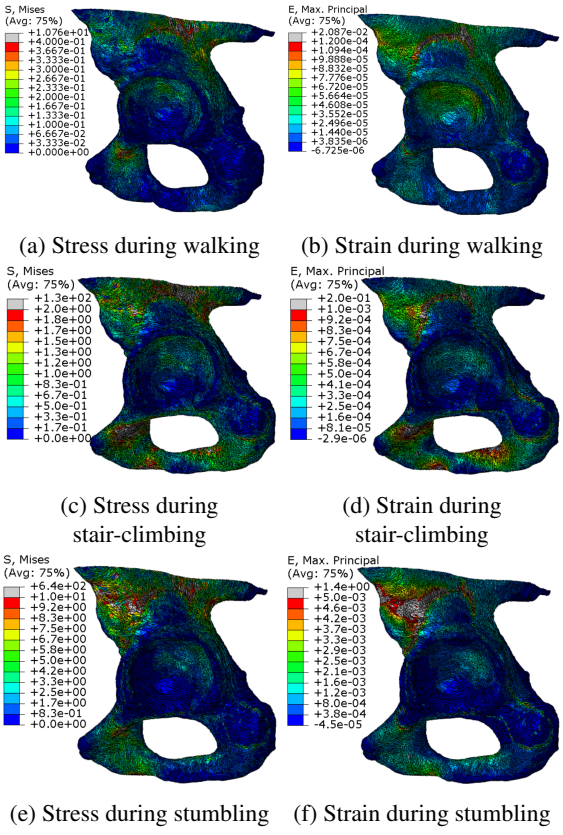

(a) Stress during walking (b) Strain during walking

(c) Stress during stair-climbing (d) Strain during stair-climbing

(e) Stress during stumbling (f) Strain during stumbling

Figure 29: Stresses and strains of the pelvis (with triflange cup implant) during different loading cases

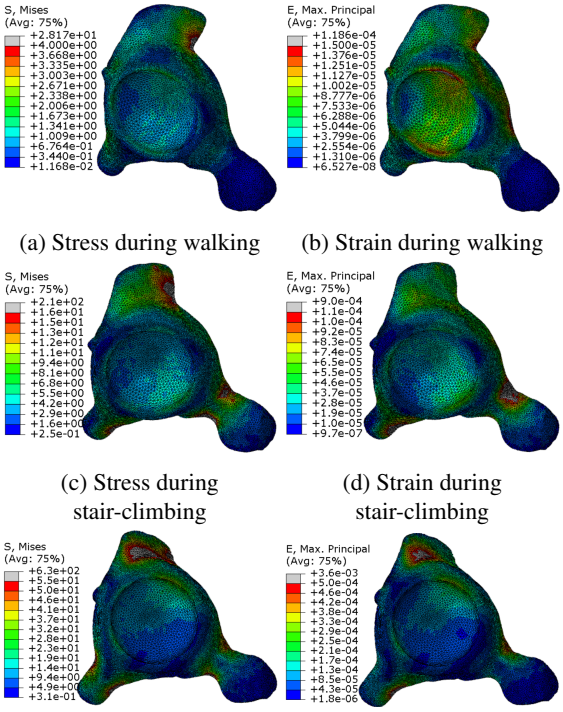

(a) Stress during walking (b) Strain during walking

(c) Stress during stair-climbing (d) Strain during stair-climbing

(e) Stress during stumbling (f) Strain during stumbling

Figure 30: Stresses and strains of the triflange cup during different loading cases

4.3: Validation of the bone-remodelling algorithms

This sections displays the results of the two validation steps for both bone-remodelling models, which is an indication of the accuracy.

4.3.1: Comparing predictions with real values

For the first validation, the bone-remodelling algorithms were validated by performing a simulation of a pelvis without implant. An initial homogeneous Youngs's modulus was applied to the whole pelvis. It was found that after +- 1 year (320 days) a steady-state was reached for the BMD, i.e. adjustments of the BMD stayed within the pre-defined boundary (figure 31).

Once the simulation was finished, BMD-values of the FE-model were obtained at different z-coordinates (heights) in the acetabulum. In addition, the acetabulum was split-up in four slices (figure 32). In each slide, 3 evenly-spaced BMD-values were obtained. Averaging these 3 values resulted in the mean BMD of each slice at a certain height. The percentual error of both models is constructed (figure 33). A boxplot displaying the BMD-values for both models, together with the actual values (from Mimics) is presented in figure 34. It can be seen that model A predicts the BMD overall in an accurate manner, but has some extreme errors for certain areas. Model B on the other hand

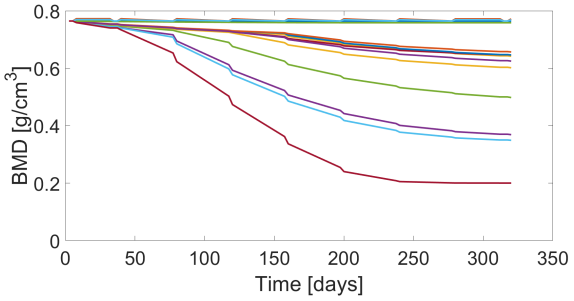

Figure 31: A steady state for all elements is reached after 320 days

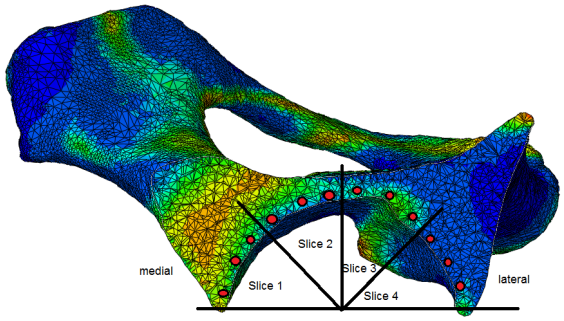

Figure 32: Top-view of the pelvis with the corresponding slices with dots representing the measurement-locations

predicts the overall BMD in a more robust manner compared to model A. The average percentage error for model A and B are 14% (+-28) and 24% (+-24) respectively.

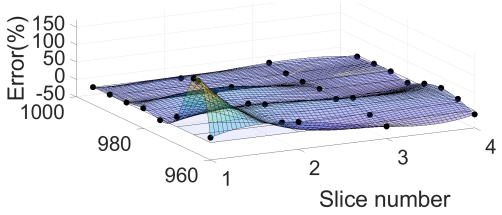

(a) Error of model A

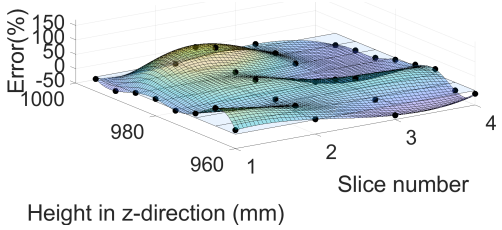

(b) Error of model B

Figure 33: Error of both bone-remodelling models (in %)

Furthermore, it becomes evident that for slice 1 and 4 the models can calculate the BMD quite well. For slice 3, the results are less accurate but still in the same range. For slice 2 however, both models deliver values which are

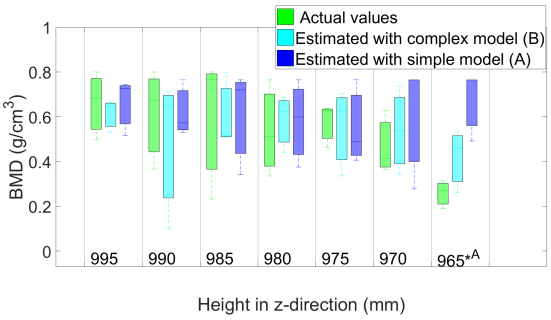

(a) Slice 1

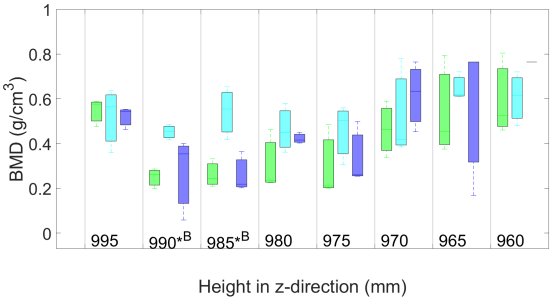

(b) Slice 2

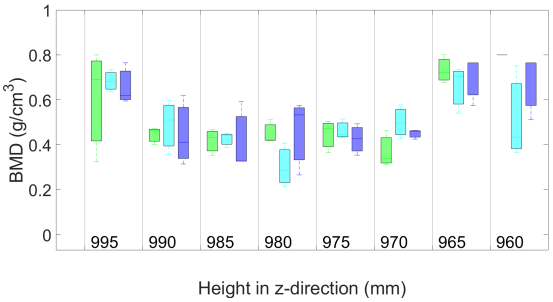

(c) Slice 3

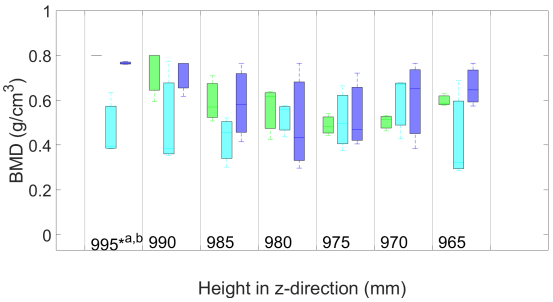

(d) Slice 4

Figure 34: Boxplot of real BMD-values of the pelvis along with the predictions of the model. $*_A$ and $*_B$ indicate a statistical difference ($p<0.05$) between the real values and predicted values from model A or B respectively

substantially off compared to the actual values. This is especially present in the higher areas.

Overall, both models show with the selected parameters sufficiently accurate results. An unpaired t-test was performed to determine if the difference between model-

predictions and real values were statistically different. Out of the 30 measurements, only 2 values for model A and 3 values for model B are statistically different from the real values from Mimics ($p<0.05$), indicated with a star in figure 34.

4.3.2: Comparing predictions with literature

Here, the results of the 2D block model are compared with the literature. In figure 35 , the results are shown for the case with the most correspondece.

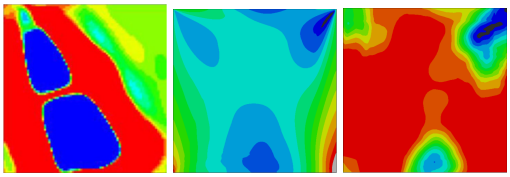

(a) Result from literature [71] (b) Result with model A (c) Result with model B

Figure 35: BMD-patterns of both models compared with literature)

For this, the chosen k-values were chosen as 20 elements. With a element size of 0.005mm, this corresponds to k-values of 0.1mm. For model B, the value of D (which determines the rate of spatial decay) was chosen as 0.050. It can be seen that overall somewhat similair patterns can be seen , with two oval areas of low BMD-values surrounded by an area of higher BMD and again a low BMD in the top-right corner. It can be seen that with lower values of D and k, less correspondence is observed (fig 36). Note that the result of model A didn't change, since by default the result of every element is only determined by the stimulus signal of that particular element.

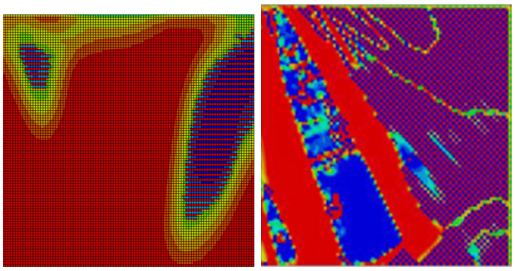

(a) Result from model B D=0.001 (b) Result from literature with D=0.001

Figure 36: BMD-patterns with a low value of D)

4.4: Prediction of BMD-values of pelvises with implants

BMD-values of the pelvis were predicted for a healthy pelvis with standard and triflange implant and for a defect pelvis with triflange and deformed implant. In this stage, k-values were chosen as 0, since the computational effort was too large otherwise. Furthermore, larger k-values resulted in less accurate results.

4.4.1: Healthy pelvis with standard and triflange implant

After validation of the models, simulations were performed to predict the BMD-values of the pelvis with the standard and triflange implant. The exact same parameters were used for every scenario (no implant, standard implant and triflange implant). This was done in order to ensure that BMD-differences were purely caused by an altered strain-magnitude and strain-distribution. Figure 37 displays the BMD-distribution for each model and each scenario.

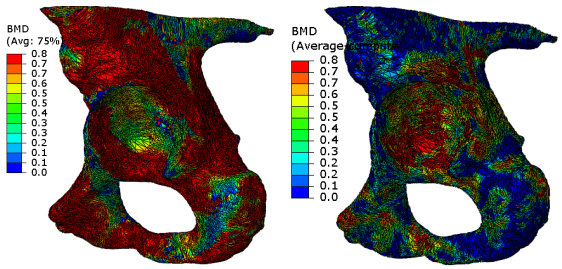

(a) Model A without implant (b) Model B without implant

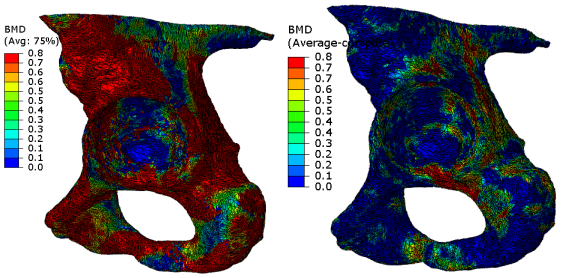

(c) Model A with standard implant (d) Model B with standard implant

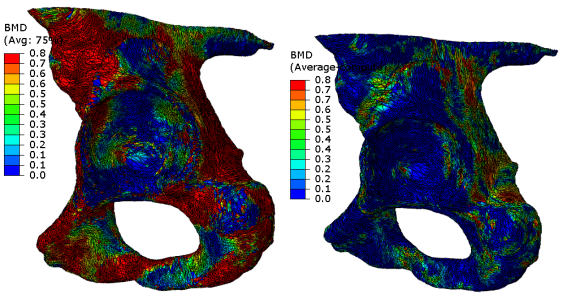

(e) Model A with triflange implant (f) Model B with triflange implant

Figure 37: BMD-distribution in the pelvis

It can be seen that the BMD-values for model B are significantly higher than for model A, even in the case without implant. Although the magnitudes are different between both models, it can be seen that the pattern of the

stress-shielding is somewhat similair. In addition, it can be seen that both models show an overall decrease in BMD between the case without implant and the case with standard implant. Similarly, a decrease in BMD is seen for the case with triflange-implant compared to the other 2 cases.

To quantify amount of stress-shielding, BMD-values were obtained at each slice and height. The approach was similair to the measurements during model-validation. Figure 38 and 39 display the average change in BMD (in %) for each location, compared to the pelvis without implant.

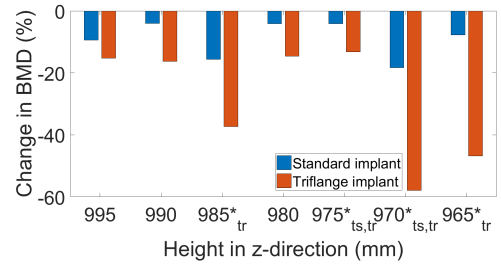

(a) Slice 1

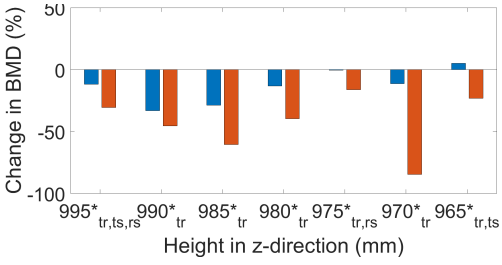

(b) Slice 2

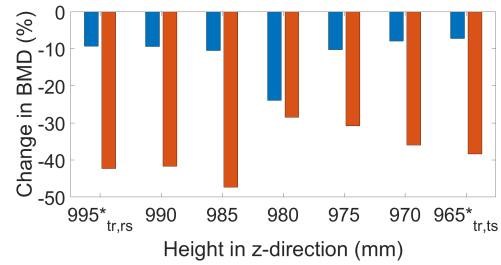

(c) Slice 3

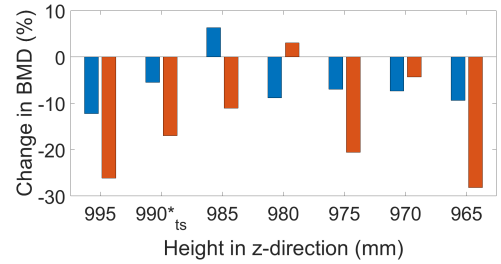

(d) Slice 4

Figure 38: Model A: Predictions in change of BMD with respect to the pelvis without implant. $*_{tr}$, $*_{ts}$ and $*_{rs}$ indicate a significant difference between triflange-no implant, triflange-standard implant and standard implant-no implant respectively.

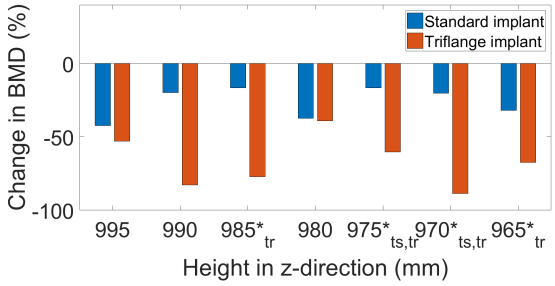

(a) Slice 1

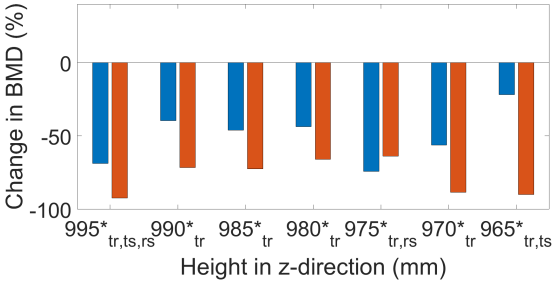

(b) Slice 2

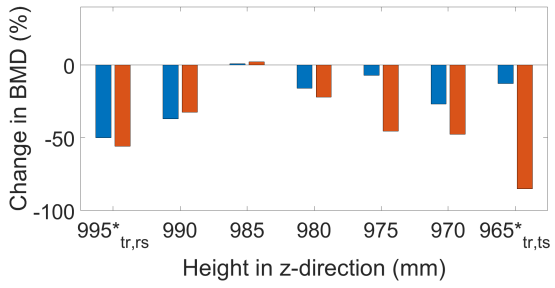

(c) Slice 3

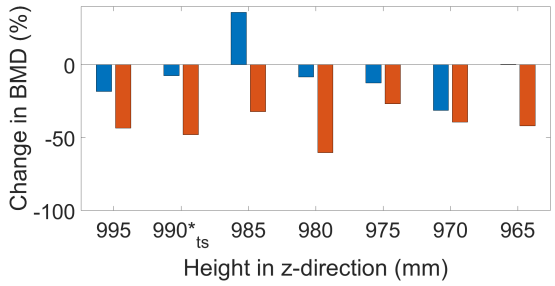

(d) Slice 4

Figure 39: Model B: Predictions in change of BMD with respect to the pelvis without implant. $*_{tr}$, $*_{ts}$ and $*_{rs}$ indicate a significant difference between triflange-no implant, triflange-standard implant and standard implant-no implant respectively.

For model A it can be seen that the decrease in BMD for the cases with implants is quite similair for every slice. Especially at the lower z-heights (z=965mm and z=970mm) a steep decrease in BMD is found for the triflange-implant. For model B, the decrease in BMD is substantially more with both implants at slice 1,2 and 4.

The average BMD-value of each case is calculated, as

can be seen in table 11. Taking all values into account for model A, it can be seen that the average BMD of a pelvis without implant is 0.56. With a standard implant, this average BMD decreases with 8.9% to a value of 0.51, which is not a significant decrease (p=0.1706, p<0.05 for significance). With a triflange implant, the BMD decreases with 28.6% with respect to the case with no implant, resulting in a value of 0.40. This decrease is significant with respect to the case without implant (p=0.0074) and with respect to the case with standard implant (p=<0.001). Doing the same for model B gives for the case without implant an average BMD of 0.52. With a standard implant, this BMD decreases with 25.0% to a value of 0.39, which is a significant decrease (p<0.001). With a triflange implant, the BMD decreases with 55.8% with respect to the case with no implant, resulting in a value of 0.23. This decrease is significant with respect to the case without implant (p=<001) and with respect to the case with standard implant (p=<0.001).

Table 11: Average BMD-values for the healthy pelvis

Average-BMD-values (g/cm^3)	*Without implant*	*Standard-implant*	*Triflange-implant*
Model A	0.56	0.51	0.40
Model B	0.52	0.39	0.23

4.4.2:Defect pelvis with triflange and deformed implant

For the defect pelvis, the BMD is calculated after 320 days for both the case with the triflange implant and the deformed implant. Since it was found that for the healthy pelvis model B underestimates the BMD-values, only model A was used for the defect pelvis, to save computational time. The BMD-values are displayed in figure 40.

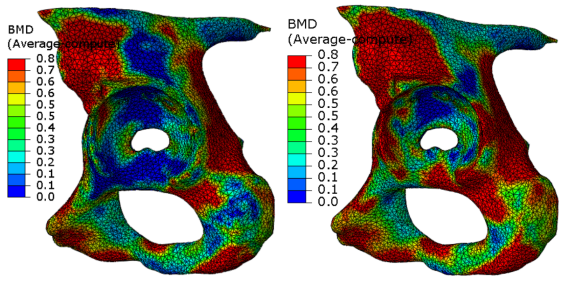

(a) Triflange implant (b) Deformed implant

Figure 40: BMD-values for the damaged pelvis

By applying the same procedure as during the validation-step, BMD-values are obtained at multiple locations. Averaging these values results in the mean BMD for both cases, which are shown in table 12. It can be seen that the triflange implant results in similair BMD-values as the healthy pelvis with triflange implant. Moreover, the deformed implant shows BMD-values which are very similar to the standard cup in the healthy pelvis. This indicates that the deformed implant can minimize the stress-shielding, reducing it to the amount of stress-shielding which occurs with the standard implant.

Table 12: Average BMD-values for the damaged pelvis

Average-BMD-values (g/cm^3)	*Without implant*	*Deformable-implant*	*Triflange-implant*
Model A	0.56	0.52	0.39

4.5: The deformable implant

This sections displays the performance results and machine-learning algoritm of the deformable implant.

4.5.1: Performance results

In total, 18 pelvises with different types of defects were evaluated. For each pelvis, analyses were performed with multiple deformable cups, which varied in thickness and interference fit. For two pelvises, the deformation process of the best-performing cup is shown (figure 41).

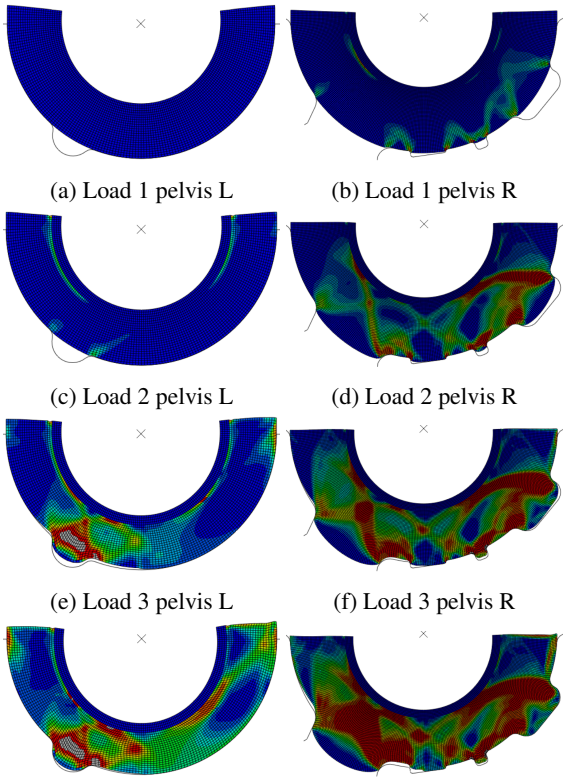

(a) Load 1 pelvis L (b) Load 1 pelvis R

(c) Load 2 pelvis L (d) Load 2 pelvis R

(e) Load 3 pelvis L (f) Load 3 pelvis R

(g) Load 4 pelvis L (h) Load 4 pelvis R

Figure 41: Deformation after each load

It can be seen that one pelvis contains a lot of damage (pelvis R) and one pelvis (pelvis L) contains a minimal amount of damage. Furthermore, the performance (and the four subvariables) were measured for each type of deformable cup. Figure 42 displays these measurements, which are the results of the same pelvises as displayed in figure 41 (i.e. pelvis L and R).

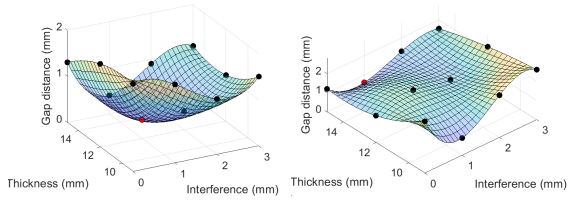

(a) Gap-distance pelvis L

(b) Gap-distance pelvis R

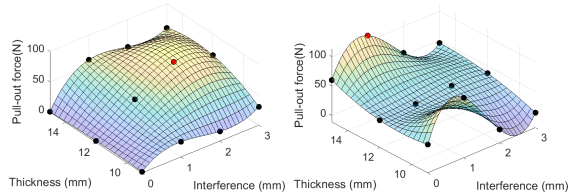

(c) Pull-out force pelvis L

(d) Pull-out force pelvis R

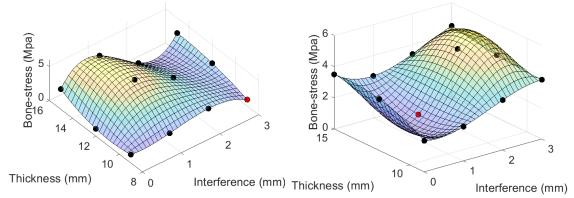

(e) Bone-stress pelvis L

(f) Bone-stress pelvis R

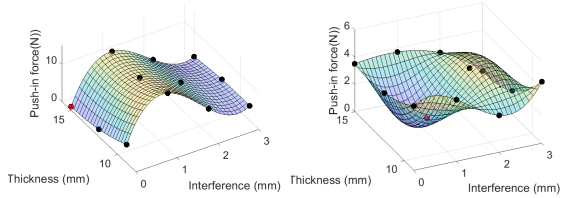

(g) Push-in force pelvis L

(h) Push-in force pelvis R

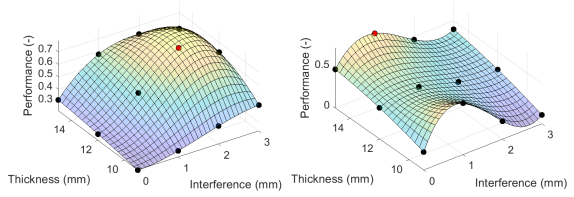

(i) Performance pelvis L

(j) Performance pelvis R

Figure 42: Performance parameters

An important finding is that the optimal performance of the deformable cup is different for each case. For pelvis L, the optimal cup has a thickness of 12mm and an interference fit of 2mmm, while for pelvis R this is a thickness of 15mm and an interference fit of 1mm. This indicates that a deformable cup with varying parameters is needed for different type of defects.

4.5.2: Machine-learning algorithm

The machine learning algorithm was trained to select the optimal cup based on the defects in the pelvis. The training data together with the optimal cup is shown in figure 43a

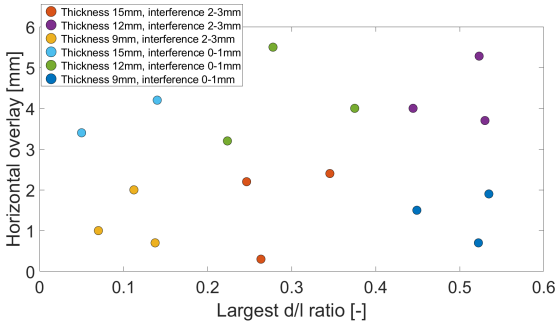

(a) Training data

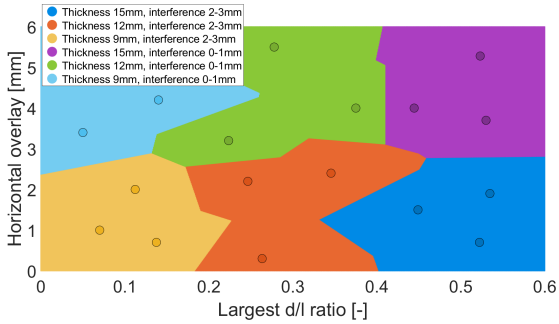

(b) Training data with classification boundaries

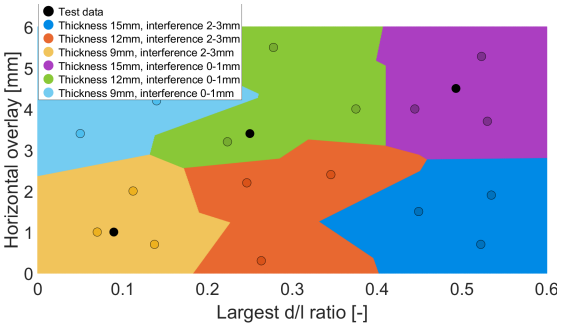

(c) Classification of test data

Figure 43: Nearest neighbour classifier to determine the optimal cup based on the bone defects

It can be seen that based on the parameters of the defect, a different optimal cup can be found. In total, six different cup designs are available. The nearest neighbour algorithm is trained based on the available training points. The boundary of each class is shown in figure 43b. The results of the FE-models of the training data is displayed in appendix D.

Finally, to test if the classification is correct, the test data was utilised. The 3 new points were added to the

machine-learning algorithm, which then predicted the optimal cup based on the parameters (figure 43c).

With the predicted optimal cup for the test data, Finite-element analysis was performed. It can indeed be seen that with this predicted optimal cup, favourable results can be obtained (figure 44). A good contact between bone and implant is obtained at the interface. The cup deforms into the defects in all cases. Based on this, it can be seen that the classifier makes a good prediction of the optimal cup. A pattern can be seen where a larger horizontal overlay and a larger d/l ratio require a cup with a smaller interfence fit and a thicker deformable layer respectively.

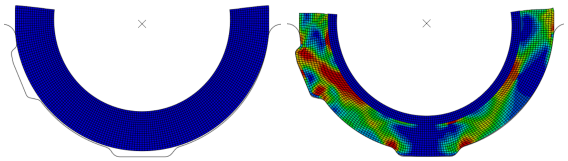

(a) Test 1: Thickness 9 interference 2 before deformation

(b) Test 1: Thickness 9 interference 2 after deformation

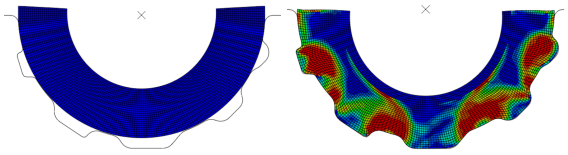

(c) Test 2: Thickness 12 interference 1 before deformation

(d) Test 2: Thickness 12 interference 1 after deformation

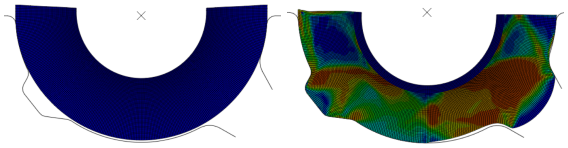

(e) Test 3: Thickness 15 interference 1 before deformation

(f) Test 3: Thickness 15 interference 1 after deformation

Figure 44: FE-results of test data

5: Discussion

5.1: Main findings

The statistical shape model of the healthy pelvis provides main modes of deviation that describe the thickness and shape at multiple locations. Overall, the deviation for each mode is quite subtle, which generates promising and realistic shapes. The six main modes occur at expected locations, namely at transitions from one bone area to another. The deviation at the acetabulum is relatively low, which is expected since the size-aspect is corrected for. However, for the first mode it can be seen that the deviation is amplified as a result of the cutting process at this area, which generated higher variations than in reality. In a next iteration, it is recommended to make a universal cut at this area, to eliminate this contribution to the variation. The statistical shape model of the defect pelvis provides main modes which are more concentrated around one area, namely the defects in the acetabulum. This is expected, since large variations are located here. However, the generated shapes are quite unrealistic and inaccurate. It is expected that this is the result of a very low amount of data in combination with a huge amount of deviation. To obtain accurate results in further research, it is recommended to obtain more data with pelvises that are somewhat less damaged, in order to minimize the amount of variation. Another option is to develop a SSM of pelvises which have somewhat the same type of defect, to minimize variation. It might also be wise to develop a model of only males or only females, since some differences in pelvic shapes exist between these groups. Comparing results with literature is difficult since most studies on SSM of the pelvis include the whole pelvis and find main modes on locations which are not included in this model [72],[73],[74]. However, most modes on areas which are included in this model show correspondence with literature. Only mode 1 is significantly different (due to the cutting, as explained earlier) and mode 20 is more excessive compared to literature, which might be caused by the settings during image segmentation from the CT-scans. The generality and specify of the healthy model are similair or even better than other models [72]. The behaviour of generality and specificity as a function of modes is as expected: More modes allow the model to create more complex shapes, while more modes also create shapes with less correspondence to the training shapes.

With the finite element model, the stresses and strains for the healthy pelvis depend on the loading scenario and type of implant, with values up till 9 Mpa and 0.009 are found respectively. The distribution of the loads are dependent on the type of loading scenario. The most important finding is that the strains and stresses decrease with a standard implant, compared to the pelvis without implant. With a triflange implant, these values decrease even further. This indicates that a higher amount of stress-shielding occurs with the triflange implant compared to the standard implant, which is in agreement with the hypothesis and literature [21] [25]. The results seem reliable, since the stresses do not exceed the yield strength, but do stimulate the pelvis with a realistic amount of stress. For a next step, it can be useful to perform the analysis of the triflange implant with screws. For now, a single simulation with screws was done, to validate that the screws do not influence the results significantly. However, this has not been adapted to the full analysis for now.

The bone remodelling algorithms that were implemented provided results which are in correspondence with the real pelvis from mimics. Model A and B provided in only 2 and 3 measurements (out of 30) a statistical difference with values from Mimics, respectively. However, for the

predicted BMD-values with the implants, model B showed values which are most likely too low, since these values would result in serious problems for the patient. It is expected that during validation, the parameters of model B were fitted for one case and do not perform well yet for other cases. Furthermore, due to computational limitations the k-values were set to 0 while the optimal value during validation of the 2D cube was determined as 15, which could cause the inaccuracy of the results. The patterns for this cube are different that the results from literature, but overall the same components can be identified. Furthermore, the model from literature is constantly optimized with neural networks, while for the models in this study this is limited to trial and error. For a next iteration, it is therefore recommended to implement an optimization of the bone-remodelling models. Model A shows more accurate results than model B. However, it is believed that this is not necessary due to model A being better than model B, but that model A is more prone to finding the correct parameters due to the relative simplicity of the model. Therefore, the results of model A are for now considered to be more accurate.

The predicted BMD-values for the healthy pelvis are lower with a standard implant than for a pelvis without implant. With a triflange implant, these BMD-values are even lower. From this it can be concluded that the triflange implant causes indeed more stress-shielding than the standard implant. This is in agreement with the hypothesis and literature [21] [25]. The decrease in BMD for the standard hemispherical cup is in this study a bit lower than the experimental measures from literature, where in some areas decreases up till 40% are reported [75]. However, the 40 % reported in literature is an = outlier and for most areas the values do show correspondence. For the custom triflange cup, limited data is available on the amount of BMD reduction. This makes it difficult to validate the results from this study. Most studies focus on the perfomance and HIP-scores, but do not specify the amount of bone absorption. However, it is mentioned that with a triflange implant bone-resorption is initiated for almost all patients [76].

The deformable implant minimizes the stress-shielding and performs on this aspect just as well as the standard cup. This is in agreement with literature, since a good connection between bone and implant is required to minimize stress-shielding [56]. For the deformable implant, it can be seen that the performance depends on parameters such as the amount of interference and the thickness. The gap distance after deformation is quite low, which shows that the cup is capable of deforming into the defect and provide a solid transition between pelvis and implant. The pull-in force and stress at the bone-interface stay within tolerable values. Only the pull-out force is lower than expected, taking values up till 110N. For standard cups, this value is around 77N-800N [65]. This relatively low value indicates that the cup is somewhat stable in the acetabulum, but a higher value is desired. However, it is expected that in reality the pull-out force might be higher, since the sharp unit-cell structure can penetrate the bone, which generates a higher pull-out force. In the simulation, the bone was modelled as incompressible and the sharp unit cell-structure was modelled as a solid section, which could lead to a pull-out force which is lower than expected. Therefore, it is important to test this experimentally and compare these to the FE-model results. An important finding is that for different types of defects, a different deformable cup provides the optimal solution. The machine learning algorithm provides a good solution, since it can determine the best cup based on the type of defects. After testing the algorithm, this method is proven to be a good approach. A pattern can be seen where defects with a larger d/l ratio require a cup with a thicker deformable layer. This can be explained by the fact that for more deformation, more material is needed to cover the defect. Moreover, defects with a smaller d/l ratio require a thin deformable layer, since with a thick layer not enough plastic deformation is initiated (i.e. there is too much material and too little deformation), causing spring-back and thus a less stable cup. In addition, pelvises with a low amount of horizontal overlay require a larger amount of interference. A larger interference fit initiates more deformation and thus a better fixation, which is desired if there is not sufficient horizontal overlay in the pelvis which prevents the cup from being pulled out of the acetabulum. With a lot of horizontal overlay however a low interference is desired, since deformation of the cup should not occur until it has reached the location of the defect.

Nevertheless, bigger test and training sets can be a good step for a next study, to further improve the algorithm. In addition, more parameters for classification of the defects can be used. However, this drastically increases the amount of computational time, which is why for now the amount of parameters is limited to two.

5.2: Evidence

The amount of evidence is considered to be sufficient for the majority of the results. Overall, most results that were found are either compared with experimental results, validated during a validation step, or compared to other studies as discussed in the previous paragraph. This provides sufficient evidence for the findings. However, there are some results which are not in agreement with previous studies and are thus considered as inaccurate with insufficient amount of evidence. This applies to the SSM of the defect pelvis, some modes of the SSM of the healthy pelvis and bone remodelling model B, as highlighted in the previous section. Furthermore, the deformable cup is a new concept, which makes it difficult to compare to literature. Therefore, it is important that these results are compared with experimental results.

5.3: Limitations

The two greatest limitations during this study are directly related to the lack of evidence for above-mentioned aspects. First, the inaccuracy of the results of bone remodelling model B is caused by incorrect parameter-values. This in turn is the result of limited computational time. To find the optimal parameters, an optimization problem should be included. However, this iterative process requires lots of simulations. With each simulation taking more than 20 hours to complete, this is for now not achievable. In the future, it can be worthwhile to optimize and simplify the FE-model, to reduce computational time per run. Then, a neural network algorithm can be implemented to find the optimal parameter values, which will then result in more accurate and realistic results. Second, the inaccurate results of the statistical shape model of the defect pelvis are caused by insufficient data. Unfortunately, a limited amount of defect pelvises were available. For a future study, the sample size should be increased. Preferably, the amount of variation at the defect should also be smaller, to allow a more accurate alignment procedure.

6: Conclusion

At first glance the custom triflange cup appears to be a convenient solution for pelvises with large bone defects. However, the implant has some drawbacks, namely the high costs and the time-consuming design-process that come with it. [19]. In addition, it was expected that the triflange implant causes more stress-shielding than a standard implant. In this study it was proven that the triflange implant causes indeed more stress-shielding than the standard cup. The triflange implant decreases the BMD of the pelvis with 28.6% compared to a pelvis with the standard implant, while this is only around 8.9% with a standard implant. To overcome the above-mentioned drawbacks, the potential of a deformable implant for large bone-defects was evaluated. It is shown that a defect pelvis with a deformable implant can reduce the stress-shielding to the same level as a healthy pelvis with the standard hemispherical cup (namely only a decrease in BMD of +- 7%). Furthermore, it is shown that the deformable cup is able to deform into multiple type of defects and obtain a sufficient initial stability. The machine-learning algorithm that was developed performs quite well and can predict the optimal cup parameters based on the defects in the pelvis. Moreover, it was shown that the statistical shape model of a pelvis can contribute to finding patterns in defects, which could eliminate the need for a customized implant.

Overall, it can be concluded that the the combination of above-mentioned aspects can potentially provide a good alternative solution for pelvises with large defects. The concept of the deformable cup together with the Statistical shape model provides solutions for the drawbacks of the triflange custom cup, which is shown in figure 45.

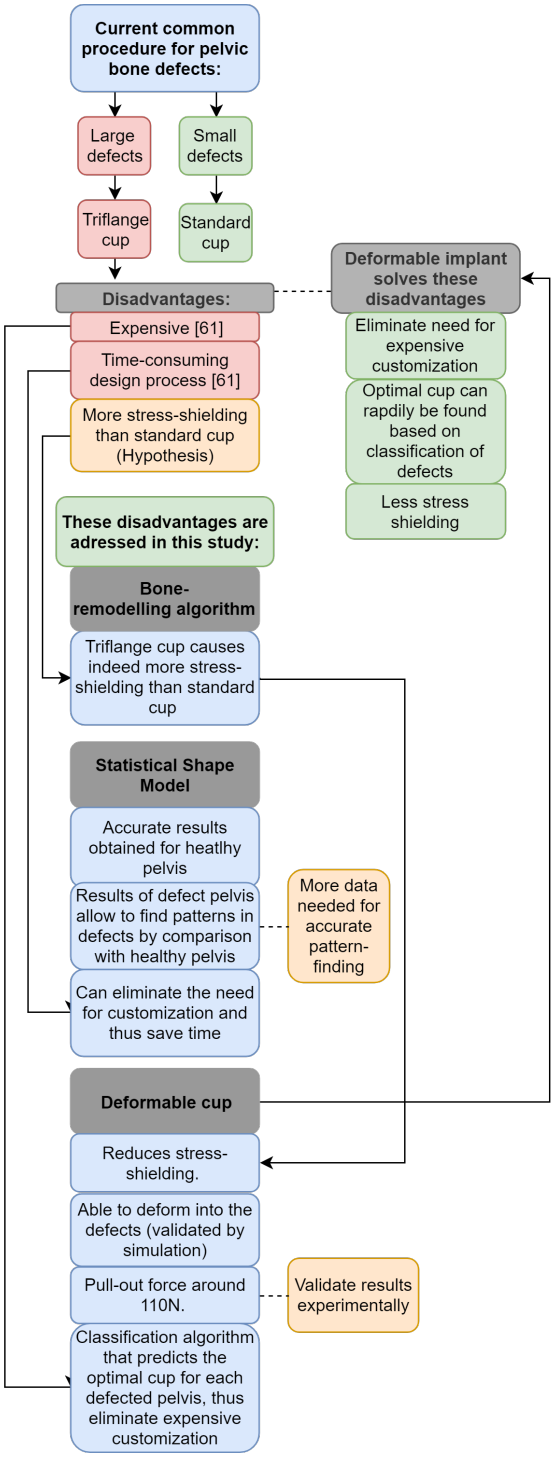

Figure 45: Overview of findings

However, more data of defect pelvises is required in order to obtain accurate modes of deviation. Furthermore, it is important to validate all results experimentally, since this study is limited to (FE-) models. After these results have indeed been validated by performing experimental results, it is believed that the deformable cup can achieve

a longer implant-life as a result of minimization of the stress-shielding. Furthermore, elimination of the customization aspect is believed to be beneficial, since it saves time and costs. With the rising costs of healthcare, this is an important advantage [23].

References

[1] Kellgren, J. H., & Lawrence, J. S. (1957). Radiological assessment of osteo-arthrosis. Annals of the rheumatic diseases, 16(4), 494

[2] david t. felson; epidemiology of hip and knee osteoartrritis , Epidemiologic Reviews, Volume 10, Issue 1, 1 January 1988, Pages 128

[3] Ganz, R., Parvizi, J., Beck, M., Leunig, M., Ntzli, H., & Siebenrock, K. A. (2003). Femoroacetabular impingement: a cause for osteoarthritis of the hip. Clinical Orthopaedics and Related Research, 417, 112-120.

[4] Landgren, E., Bremander, A., Lindqvist, E., Van der Elst, K., Larsson, I. (2018). FRI0707-HPR Patients experiences of health in early rheumatoid arthritisa qualitative study.

[5] McCollum, D. E., Nunley, J. A., & Harrelson, J. M. (1980). Bone-grafting in total hip replacement for acetabular protrusion. The Journal of bone and joint surgery. American volume, 62(48), 1065-1073.

[6] Wang, W., Yeung, K. W. (2017). Bone grafts and biomaterials substitutes for bone defect repair: A review. Bioactive materials

[7] Taunton, M. J., Fehring, T. K., Edwards, P., Bernasek, T., Holt, G. E., & Christie, M. J. (2012). Pelvic discontinuity treated with custom triflange component: a reliable option. Clinical Orthopaedics and Related Research, 470(2), 428-434.

[8] Tsao, A. K., Roberson, J. R., Christie, M. J., Dore, D. D., Heck, D. A., Robertson, D. D., & Poggie, R. A. (2005). Biomechanical and clinical evaluations of a porous tantalum implant for the treatment of early-stage osteonecrosis. JBJS, 87, 22-27.

[9] Kurtz, S., Ong, K., Lau, E., Mowat, F., & Halpern, M. (2007). Projections of primary and revision hip and knee arthroplasty in the United States from 2005 to 2030. JBJS, 89(4), 780-785.

[10] Rajaee, S. S., Campbell, J. C., Mirocha, J., & Paiement, G. D. (2018). Increasing burden of total hip arthroplasty revisions in patients between 45 and 64 years of age. JBJS, 100(6), 449-458.

[11] Antonovsky, A. (1967). Social class, life expectancy and overall mortality. The Milbank Memorial Fund Quarterly, 45(2), 31-73.

[12] Aldinger, P. R., Thomsen, M., Mau, H., Ewerbeck, V., & Breusch, S. J. (2003). Cementless Spotorno tapered titanium stems: excellent 10-15-year survival in 141 young patients. Acta Orthopaedica Scandinavica, 74(3), 253-258.

[13] Sumner, D. R. (2015). Long-term implant fixation and stress-shielding in total hip replacement. Journal of Biomechanics, 48(5), 797-800.

[14] Rubin, C. T., Lanyon, L. E. (1985). Regulation ofbone mass by mechanical strain magnitude. Calcifiedtissue international, 37(4), 411-417.

[15] Kim, Y. H., Yoon, S. H.,Kim, J. S. (2007).Changes in the bone mineral density in the acetab-ulum and proximal femur after cementless total hipreplacement: alumina-on-alumina versus alumina-on-polyethylene articulation. The Journal of bone andjoint surgery. British volume, 89(2), 174-179

[16] Huiskes, R., Weinans, H.,Van Rietbergen, B.(1992). The relationship between stress shielding andbone resorption around total hip stems and the effectsof flexible materials. Clinical orthopaedics and relatedresearch, 124-134

[17] Ruff, C., Holt, B., Trinkaus, E. (2006). Whos afraidof the big bad Wolff?:Wolffs law and bone functionaladaptation. American Journal of Physical Anthropol-ogy: The Official Publication of the American Asso-ciation of Physical Anthropologists, 129(4), 484-498.

[18] Niinomi, M., Nakai, M. (2011). Titanium-based biomaterials for preventing stress shielding between implant devices and bone. International journal of biomaterials, 2011

[19] Zivkovic, I., Gonzalez, M., Amirouche, F. (2010).The effect of under-reaming on the cup/bone interfaceof a press fit hip replacement. Journal of Biomechan-ical Engineering, 132(4), 041008.

[20] Harrysson, O. L., Hosni, Y. A., & Nayfeh, J. F. (2007). Custom-designed orthopedic implants evaluated using finite element analysis of patient-specific computed tomography data: femoral-component case study. BMC musculoskeletal disorders, 8(1), 91

[21] Cilingir, A. C., Ucar, V., Kazan, R. (2007). Three-dimensional anatomic finite element modelling ofhemi-arthroplasty of human hip joint. Trends Biomater Artif Organs, 21(1), 63-72

[22] Oki, H., Ando, M., Omori, H., Okumura, Y., Negoro,K., Uchida, K., Baba, H. (2004). Relation BetweenVertical Orientation and Stability of Acetabular Com-ponent in the Dysplastic Hip Simulated by NonlinearThreedimensional Finite Element Method. Artificialorgans, 28(11), 1050-1054

[23] Cauchi, D., & Garcia, A. (2018, April 12). health insurance: premiums and increases. Retrieved March 7, 2019, from http://www.ncsl.org/research/health/health-insurance-premiums.aspx

[24] Mclaughlin, J. R., Harris, W. H. (1996). Revision ofthe Femoral Component of a Total Hip Arthroplastywith the Calcar-Replacement Femoral Component.:Results After a Mean of 10.8 Years Postoperatively.JBJS, 78(3), 331-339.

[25] Wong, K. C., Kumta, S. M., Geel, N. V., Demol,J. (2015). One-step reconstruction with a 3D-printed,biomechanically evaluated custom implant after com-plex pelvic tumor resection. Computer Aided Surgery,20(1), 14-23.

[26] Brown, K. M., Handa, V. L., Macura, K. J., & DeLeon, V. B. (2013). Three-dimensional shape differences in the bony pelvis of women with pelvic floor disorders. International urogynecology journal, 24(3), 431-439.

[27] Subburaj, K., Ravi, B., & Agarwal, M. (2009). Automated identification of anatomical landmarks on 3D bone models reconstructed from CT scan images. Computerized Medical Imaging and Graphics, 33(5), 359-368.

[28] Clogenson, M., Duff, J. M., Luethi, M., Levivier, M., Meuli, R., Baur, C., & Henein, S. (2015). A statistical shape model of the human second cervical vertebra. International journal of computer assisted radiology and surgery, 10(7), 1097-1107.

[29] Ward, C. V., Maddux, S. D., Middleton, E. R. (2018). Threedimensional anatomy of the anthropoid bony pelvis. American journal of physical anthropology, 166(1), 3-25.

[30] Ross, A. (2004). Procrustes analysis. Course report, Department of Computer Science and Engineering, University of South Carolina.

[31] Lthi, M., Jud, C., & Vetter, T. (2013, September). A unified approach to shape model fitting and non-rigid registration. In International workshop on machine learning in medical imaging (pp. 66-73). Springer, Cham.

[32] Hotelling, H. (1933). Analysis of a complex of statistical variables into principal components. Journal of educational psychology, 24(6), 417.

[33] Styner, M. A., Rajamani, K. T., Nolte, L. P., Zsemlye, G., Szkely, G., Taylor, C. J., & Davies, R. H. (2003, July). Evaluation of 3D correspondence methods for model building. In Biennial International Conference on Information Processing in Medical Imaging (pp. 63-75). Springer, Berlin, Heidelberg.

[34] van de Giessen, M., Foumani, M., Streekstra, G. J., Strackee, S. D., Maas, M., van Vliet, L. J., ... & Vos, F. M. (2010). Statistical descriptions of scaphoid and lunate bone shapes. Journal of Biomechanics, 43(8), 1463-1469.

[35] Pedoia, V., Lansdown, D. A., Zaid, M., McCulloch, C. E., Souza, R., Ma, C. B., Li, X. (2015). Three-dimensional MRI-based statistical shape model and application to a cohort of knees with acute ACL injury. Osteoarthritis and cartilage, 23(10), 1695-1703.

[36] Zivkovic, I., Gonzalez, M., & Amirouche, F. (2010). The effect of under-reaming on the cup/bone interface of a press fit hip replacement. Journal of Biomechanical Engineering, 132(4), 041008.

[37] Amirouche, F., Solitro, G. F., Walia, A., Gonzalez, M., & Bobko, A. (2017). Segmental acetabular rim defects, bone loss, oversizing, and press fit cup in total hip arthroplasty evaluated with a probabilistic finite element analysis. International orthopaedics, 41(8), 1527-1533.

[38] Al-Hamad, M., Le Duff, M. J., Takamura, K. M., & Amstutz, H. C. (2014). Acetabular component thickness does not affect mid-term clinical results in hip resurfacing. Clinical Orthopaedics and Related Research, 472(5), 1528-1534.

[39] Goebel, P., Kluess, D., Wieding, J., Souffrant, R., Heyer, H., Sander, M., & Bader, R. (2013). The influence of head diameter and wall thickness on deformations of metallic acetabular press-fit cups and UHMWPE liners: a finite element analysis. Journal of Orthopaedic Science, 18(2), 264-270.

[40] Sylliaasen, S. J. (2010). The Development and Validation of a Finite Element Model of a Canine Rib For Use With a Bone Remodeling Algorithm.

[41] Martin, R. B., Burr, D. B., Sharkey, N. A., Fyhrie, D. P. (1998). Skeletal tissue mechanics (Vol. 190). New York: Springer.

[42] Dyce, K. M., Sack, W. O., Wensing, C. J. G. (2009). Textbook of veterinary anatomy-E-Book. Elsevier Health Sciences.

[43] Manley, M. T., Ong, K. L., & Kurtz, S. M. (2006). The potential for bone loss in acetabular structures following THA. Clinical Orthopaedics and Related Research, 453, 246-253.

[44] Janssen, D., Zwartel, R. E., Doets, H. C., & Verdonschot, N. (2010). Computational assessment of press-fit acetabular implant fixation: the effect of implant design, interference fit, bone quality, and frictional properties. Proceedings of the Institution of Mechanical Engineers, Part H: Journal of Engineering in Medicine, 224(1), 67-75.

[45] Zivkovic, I., Gonzalez, M., Amirouche, F. (2010). The effect of under-reaming on the cup/bone interface of a press fit hip replacement. Journal of Biomechanical Engineering, 132(4), 041008.

[46] Zhou, Y., Min, L., Liu, Y., Shi, R., Zhang, W., Zhang, H., ... & Tu, C. (2013). Finite element analysis of the pelvis after modular hemipelvic endoprosthesis reconstruction. International orthopaedics, 37(4), 653-658.

[47] Levenston, M. E., Beaupre, G. S., Schurman, D. J., & Carter, D. R. (1993). Computer simulations of stress-related bone remodeling around noncemented acetabular components. The Journal of arthroplasty, 8(6), 595-605.

[48] Hulskes, R. (1987). Finite element analysis of acetabular reconstruction: noncemented threaded cups. Acta Orthopaedica Scandinavica, 58(6), 620-625.

[49] Cilingir, A. C., Ucar, V., & Kazan, R. (2007). Three-dimensional anatomic finite element modelling of hemi-arthroplasty of human hip joint. Trends Biomater Artif Organs, 21(1), 63-72.

[50] Wong, K. C., Kumta, S. M., Geel, N. V., Demol, J. (2015). One-step reconstruction with a 3D-printed, biomechanically evaluated custom implant after complex pelvic tumor resection. Computer Aided Surgery, 20(1), 14-23.

[51] La Rosa, G., Clienti, C., Di Bella, S., & Rizza, F. (2016). Numerical analysis of a custom-made pelvic prosthesis. Procedia Structural Integrity, 2, 1295-1302.

[52] Ma, W., Zhang, X., Wang, J., Zhang, Q., Chen, W., & Zhang, Y. (2013). Optimized design for a novel acetabular component with three wings. A study of finite element analysis. Journal of Surgical Research, 179(1), 78-86.

[53] Anuca, D., Pleea, I. E., Iliescu, N., Tomescu, P., Poenaru, F., Dasclu, V., & Pop, O. T. (2006). Morphological experimental study of bone stress at the interface acetabular bone/prosthetic cup in the bipolar hip prosthesis. Romanian journal of morphology and embryology= Revue roumaine de morphologie et embryologie, 47(2), 99-111.

[54] Kluess, D., Souffrant, R., Mittelmeier, W., Wree, A., Schmitz, K. P., & Bader, R. (2009). A convenient approach for finite-element-analyses of orthopaedic implants in bone contact: modeling and experimental validation. Computer methods and programs in biomedicine, 95(1), 23-30.

[55] Voigt, C., Klhn, C., Bader, R., von Salis-Soglio, G., Scholz, R. (2007). Finite element analysis of shear stresses at the implant-bone interface of an acetabular press-fit cup during impingement/Finite-Elemente-Berechnung der Schubspannungen im Implantat-Knochen-Interface einer acetabulren Press-Fit-Pfanne bei Impingement. Biomedizinische Technik, 52(2), 208-215.

[56] Schuller, H. M., Dalstra, M., Huiskes, R., & Marti, R. K. (1993). Total hip reconstruction in acetabular dysplasia. A finite element study. The Journal of bone and joint surgery. British volume, 75(3), 468-474.

[57] Zhang, Q. H., Wang, J. Y., Lupton, C., Heaton-Adegbile, P., Guo, Z. X., Liu, Q., & Tong, J. (2010). A subject-specific pelvic bone model and its application to cemented acetabular replacements. Journal of biomechanics, 43(14), 2722-2727.

[58] Bergmann, G., Deuretzbacher, G., Heller, M., Graichen, F., Rohlmann, A., Strauss, J., & Duda, G. N. (2001). Hip contact forces and gait patterns from routine activities. Journal of biomechanics, 34(7), 859-871.

[59] Bergmann, G., Graichen, F., & Rohlmann, A. (2004). Hip joint contact forces during stumbling. Langenbeck's Archives of Surgery, 389(1), 53-59.

[60] Bergmann, G., Graichen, F., Rohlmann, A., Bender, A., Heinlein, B., Duda, G. N., ... & Morlock, M. M. (2010). Realistic loads for testing hip implants. Biomedical materials and engineering, 20(2), 65-75.

[61] Yoshida, H., Faust, A., Wilckens, J., Kitagawa, M., Fetto, J., & Chao, E. Y. S. (2006). Three-dimensional dynamic hip contact area and pressure distribution during activities of daily living. Journal of biomechanics, 39(11), 1996-2004.

[62] unknown. 2018. Human anatomy. [online] Available at: https://human.biodigital.com/. [Accessed 27 December 2018].

[63] Thompson, M. S., Northmore-Ball, M. D., & Tanner, K. E. (2002). Effects of acetabular resurfacing

component material and fixation on the strain distribution in the pelvis. Proceedings of the Institution of Mechanical Engineers, Part H: Journal of Engineering in Medicine, 216(4), 237-245.

[64] Carl, J., Mller-Hoeppe, D., Meadows, M. (2006).Comparison of tetrahedral and brick elements for linear elastic analysis. University of Colorado Boulder, Boulder, USA.

[65] Spears, I. R., Morlock, M. M., Pfleiderer, M., Schneider, E., Hille, E. (1999). The influence of friction and interference on the seating of a hemispherical press-fit cup: a finite element investigation. Journal of Biomechanics, 32(11), 1183-1189.

[66] Luo, S., Shen, X., Bai, X., Bai, J., Han, J., Shang, Y. (2017). Validation of Material Algorithms for Femur Remodelling Using Medical Image Data. Applied bionics and biomechanics, 2017.

[67] Baldini, A., Bruzzesi, G., Zaffe, D., Giacopini, M., Strozzi, A., & De Pol, A. (2008). Biomechanical aspects in dental replacements. WIT Transactions on State-of-the-art in Science and Engineering, 35, 197-243.

[68] Hazelwood, S. J., Martin, R. B., Rashid, M. M., & Rodrigo, J. J. (2001). A mechanistic model for internal bone remodeling exhibits different dynamic responses in disuse and overload. Journal of Biomechanics, 34(3), 299-308.

[69] Mow, V. C., Huiskes, R. (Eds.). (2005). Basic orthopaedic biomechanics mechano-biology. Lippincott Williams Wilkins.

[70] Mullender, M. G., Huiskes, R., Weinans, H. (1994). A physiological approach to the simulation of bone remodeling as a self-organizational control process. Journal of biomechanics, 27(11), 1389-1394.

[71] Zadpoor, A. A., Campoli, G., Weinans, H. (2013). Neural network prediction of load from the morphology of trabecular bone. Applied Mathematical Modelling, 37(7), 5260-5276.

[72] Lamecker, H., Seebass, M., Hege, H. C., Deuflhard, P. (2004, May). A 3D statistical shape model of the pelvic bone for segmentation. In Medical Imaging 2004: Image Processing (Vol. 5370, pp. 1341-1352). International Society for Optics and Photonics.

[73] Barratt, D. C., Chan, C. S., Edwards, P. J., Penney, G. P., Slomczykowski, M., Carter, T. J., Hawkes, D. J. (2008). Instantiation and registration of statistical shape models of the femur and pelvis using 3D ultrasound imaging. Medical image analysis, 12(3), 358-374.

[74] Skadubowicz, P., Krl, Z., Wrbel, Z., Hefti, F., Krieg, A. (2009). Using of statistical shape models for pelvis reconstruction in the oncologic surgery. Journal of Medical Informatics Technologies, 13.

[75] Meneghini, R. M., Ford, K. S., McCollough, C. H., Hanssen, A. D., Lewallen, D. G. (2010). Bone remodeling around porous metal cementless acetabular components. The Journal of arthroplasty, 25(5), 741-747.

[76] Berend, M. E., Berend, K. R., Lombardi, A. V., Cates, H., Faris, P. (2018). The patient-specific Triflange acetabular implant for revision total hip arthroplasty in patients with severe acetabular defects: planning, implantation, and results. The bone joint journal, 100(1_Supple_A), 50-54.